Model Assessment of Decadal Variability and Trends in the Tropical Pacific Ocean

THOMAS R. KNUTSON AND SYUKURO MANABE*

NOAA/Geophysical Fluid Dynamics Laboratory, Princeton, New Jersey

(Manuscript received 9 April 1997, in final form 10 November 1997)

ABSTRACT

In this report, global coupled ocean–atmosphere models are used to explore possible mechanisms for observed decadal variability and trends in Pacific Ocean SSTs over the past century. The leading mode of internally generated decadal (>7 yr) variability in the model resembles the observed decadal variability in terms of pattern and amplitude. In the model, the pattern and time evolution of tropical winds and oceanic heat content are similar for the decadal and ENSO timescales, suggesting that the decadal variability has a similar "delayed oscillator" mechanism to that on the ENSO timescale. The westward phase propagation of the heat content anomalies, however, is slower and centered slightly farther from the equator ($\sim 12°$ vs $9°N$) for the decadal variability. Cool SST anomalies in the midlatitude North Pacific during the warm tropical phase of the decadal variability are induced in the model largely by oceanic advection anomalies.

An index of observed SST over a broad triangular region of the tropical and subtropical Pacific indicates a warming rate of $+0.41°C$ $(100$ yr$)^{-1}$ since 1900, $+1.2°C$ $(100$ yr$)^{-1}$ since 1949, and $+2.9°C$ $(100$ yr$)^{-1}$ since 1971. All three warming trends are highly unusual in terms of their duration, with occurrence rates of less than 0.5% in a 2000-yr simulation of internal climate variability using a low-resolution model. The most unusual is the trend since 1900 (96-yr duration): the longest simulated duration of a trend of this magnitude is 85 yr. This suggests that the observed trends are not entirely attributable to natural (internal) variability alone, although natural variability could potentially account for much of the observed trends. To quantitatively explore the possible role of greenhouse gases and aerosols in the observed warming trends, two simulations (using different initial conditions) of twentieth-century climate change due to these two radiative forcings were analyzed. These simulate an accelerated warming trend [$\sim 2°C$ $(100$ yr$)^{-1}$] in the triangular Pacific region beginning around the 1960s and suggest that nearly all of the recent warming in the region could be attributable to such a thermal forcing. In summary, the authors' model results indicate that the observed warming trend in the eastern tropical Pacific is not likely to be solely attributable to internal (natural) climate variability. Instead, it is likely that a sustained thermal forcing, such as the increase of greenhouse gases in the atmosphere, has been at least partly responsible for the observed warming.

1. Introduction

An intriguing feature of the Pacific Ocean climate during the 1980s and early 1990s has been the distinctive triangular-shaped warming anomaly pattern in the tropical and subtropical Pacific, which has persisted through much of the period. This pattern is clearly apparent in a linear trend map of Pacific SSTs over the 46-yr period from 1949 to 1994 shown in Fig. 1 (see also Nitta and Yamada 1989; Parker et al. 1994; Nicholls et al. 1995; Meehl and Washington 1996). The triangular region of recent warming extends along much of the North and South American coasts in the eastern part of the basin but is confined to low latitudes near the date

line in the western Pacific. Substantial cooling trends are apparent in the central and western parts of the extratropical Pacific in both hemispheres. A number of investigators have presented evidence for coherent decadal SST variability involving the tropical and extratropical Pacific (e.g., Nitta and Yamada 1989; Graham 1994; Trenberth and Hurrell 1994; Deser and Blackmon 1995).

A time series perspective on the recent warming can be seen (Fig. 2) by averaging over the region indicated by the dark outline in Fig. 1, which we will refer to as the Triangular Pacific (TPAC) region. The 5-month running mean TPAC index (thin solid curve in Fig. 2) shows interannual fluctuations associated with El Niño–Southern Oscillation (ENSO), as seen by comparing with the NINO3 index (dashed line, scaled by the factor 0.5 to fit on the diagram). The prevalence of warm conditions in the 1980s and 1990s could be interpreted as unusually frequent and/or prolonged ENSO warm events or, alternatively, as a low-frequency (decadal scale) shift to warmer conditions in the mid-1970s (see also Gutzler 1996) as indicated by the dark solid curve

* Current affiliation: Institute for Global Change Research, Frontier Research System for Global Change, Tokyo, Japan.

Corresponding author address: Thomas R. Knutson, NOAA/GFDL, P.O. Box 308, Princeton, NJ 08542-0308.
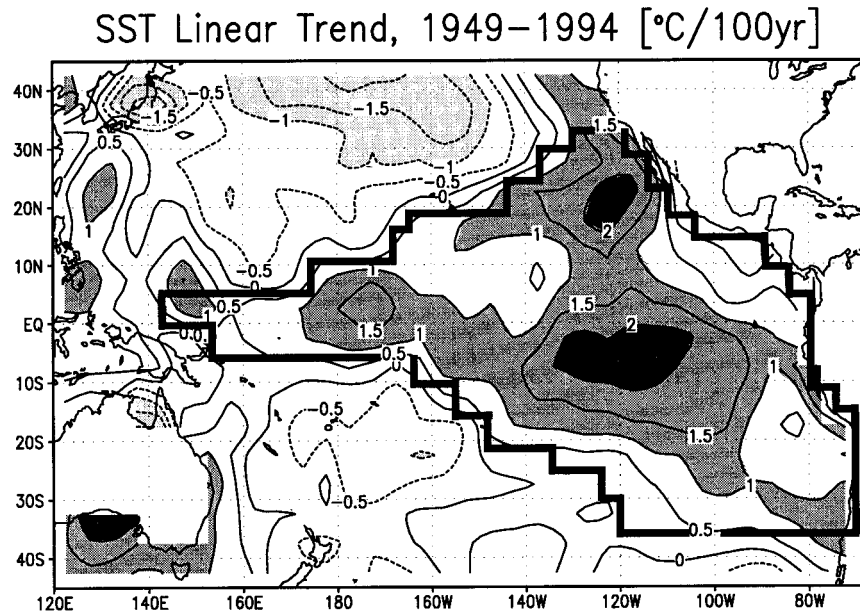E-mail: tk@gfdl.gov

FIG. 1. Linear trend in Pacific SST (1949–94) based on the GISST2 dataset (Rayner et al. 1996). Contour interval is 0.5°C (100 yr)⁻¹. The thick dark line indicates the region used to construct the Triangular Pacific index.

in Fig. 2, which is a low-pass (>7 yr) filtered version of the TPAC index.

The central motivating question for this study is, *what is the cause of the recent Pacific anomalies shown in Fig. 1*? In this report we use a series of coupled GCM experiments to study the possible roles of two potential mechanisms: 1) natural (internal) decadal-scale variability of the climate system; and 2) a sustained thermal forcing, such as that due to increased greenhouse gases and aerosols. Although our study focuses on the tropical Pacific region, the above question may also have relevance to our understanding of global SST changes since, as we will show in this study, SSTs in the TPAC region have a substantial correlation with global SSTs (see also Graham 1995 and Schneider et al. 1997).

An interpretation of the recent Pacific anomalies in terms of natural decadal variability is proposed by Zhang et al. (1997), who examined observed SSTs from 1900 to 1993. They interpret the recent Pacific pattern as primarily related to an ENSO-like variability on decadal to century timescales. Latif et al. (1997) propose that the anomalies of the 1990s in particular were associated with natural decadal variability as opposed to greenhouse warming. Recent coupled GCM studies have begun to present evidence for substantial internally generated ENSO-like decadal variability in such models. Yukimoto et al. (1996) found interdecadal Pacific variability in a 70-yr simulation of their coupled GCM; this decadal variability also had several characteristics in common with their model's simulated ENSO timescale variability. Knutson et al. (1997) found decadal-scale ENSO-like variability in their low-resolution

(R15) global coupled model, which they noted fluctuated strongly in its prominence between different centuries of a 1000-yr model integration.

An alternative view of the recent Pacific anomalies suggests a possible role for increased greenhouse gases. Transient simulations using coupled climate models indicate a substantial warming of the tropical Pacific in response to increasing greenhouse gases (Knutson and Manabe 1995; Mitchell et al. 1995; Tett 1995; Meehl and Washington 1996) or combined greenhouse gases and aerosols (Mitchell et al. 1995; Meehl et al. 1996). Meehl and Washington (1996) further argue that the linear trend over the Pacific for the period 1970–91 resembles the pattern of temperature change due to increased greenhouse gases as predicted by their coupled climate model. From an observational perspective, Trenberth and Hoar (1996) describe the recent behavior (since 1990) of the Southern Oscillation index (SOI) as unlikely to have been due to a natural climate fluctuation, based on an autoregressive time series analysis of the index. They suggest that a longer-term climate change could already be under way in the Pacific. On the other hand, Cane et al. (1997) argue that SSTs in the Pacific cold tongue region have *cooled* since 1900 and that such a response results from an ''ocean dynamical thermostat'' mechanism that is missing from current coupled GCMs.

In this report, several coupled ocean–atmosphere GCM experiments are used to explore possible mechanisms for the recent observed Pacific changes. In particular, low- and high-resolution simulations with no external forcing changes are used to study the mecha-
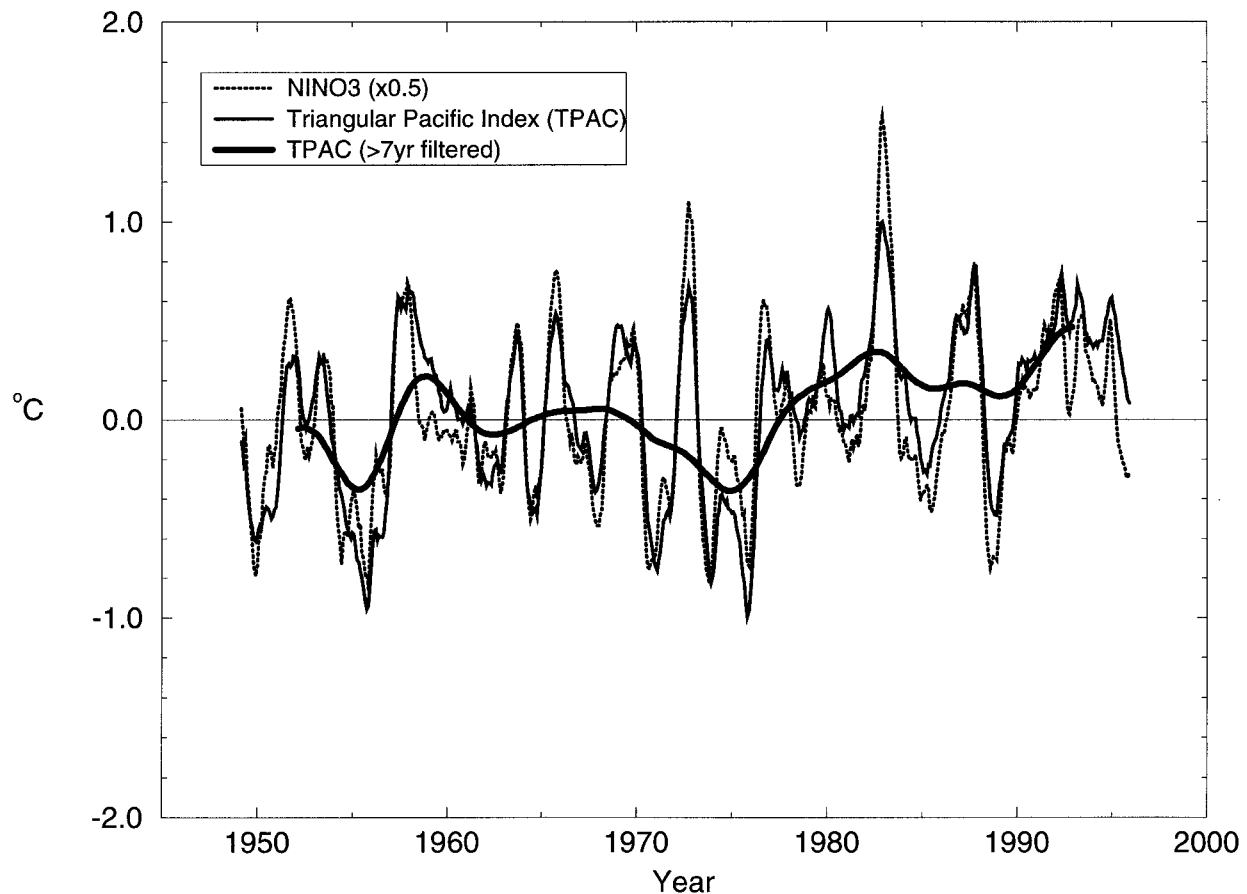
FIG. 2. Five-month running mean time series for the NINO3 region (5°N–5°S, 150°W–90°W; dotted curve) and TPAC region (thin solid line). See Fig. 1 for definition of the TPAC region. The thickest solid curve is the >7-yr filtered version of the TPAC index. The NINO3 index has been scaled by the factor 0.5 to fit on the same diagram with the TPAC curves. The SST data is from the MOHSST6 dataset (Parker et al. 1995).

nisms of internal decadal (>7 yr) variability in the Pacific and to assess the potential role of such internal variability in the observed changes. A CO_2 perturbation run with the higher-resolution model and a pair of low-resolution model simulations of twentieth-century climate change induced by estimated greenhouse gas and sulfate aerosol forcing (Haywood et al. 1997) are used to explore the possible role of these anthropogenic thermal forcings in the recent observed Pacific changes.

2. Description of models, data, and filtering

a. Model description and experiments

The primary coupled ocean–atmosphere model used here is a higher-resolution version of that described in Manabe and Stouffer (1994), and references therein. The model has interactive clouds and seasonally varying solar insolation. The atmospheric component is a global GCM, with 14 finite difference (sigma) levels in the vertical. The horizontal distributions of variables in this model are represented in both spectral and gridpoint domains (rhomboidal truncation at zonal wavenumber 30, i.e., "R30," and a 2.2° lat × 3.75° long computational grid). The model uses a new spherical harmonic representation of topography (Lindberg and Broccoli 1996) with substantially reduced "Gibbs ripples" and associated precipitation simulation artifacts. The ocean component is a global 18-level gridpoint GCM (MOM1) with 2.2° lat × 1.875° long resolution and a 32-m-thick top layer.

The model uses the flux adjustment technique for heat and salinity fluxes at the ocean surface to reduce model drift so that the CO_2 perturbations and internally generated variability occur relative to a reasonably realistic control run state (Manabe et al. 1991). For example, if tropical SSTs were allowed to drift by several degrees from the observed initial condition, the evaporative damping of SST anomalies during model ENSO events would be substantially changed, possibly distorting the model's ENSO phenomenon. The flux adjustments are determined prior to the time integration of the coupled model, and thus they are not correlated to the transient surface anomalies of temperature and salinity in the model. Despite the use of the flux adjustment, this model

shows symptoms of substantial drift, particularly in the high North Atlantic and deep Southern Ocean. However, the local SST trends in the Pacific north of about 30°S are relatively small (less than ± 0.5°C $(100 \text{ yr})^{-1}$ in most areas, and generally less than ± 0.2°C $(100 \text{ yr})^{-1}$ in the Tropics). This suggests that the current model can be used for regional Pacific studies, although we have chosen not to use it for global studies. Efforts are under way to reduce the high-latitude drift problems in the model for a future series of integrations.

Two 120-yr experiments with this higher-resolution model are used for this analysis. In the control experiment, CO_2 remains constant throughout. In the perturbation experiment, CO_2 increases at 1% yr^{-1} compounded (corresponding to an approximately linear increase in radiative forcing) with the CO_2 concentration by year 120 reaching 3.3 times that of the control experiment. To explore the role of ocean dynamics in the CO_2 response, some results are presented for comparison using an R30 mixed layer model (which by design does not include interactive ocean dynamics).

Three experiments with a lower-resolution coupled model (R15, with rhomboidal truncation at zonal wavenumber 15) are also used in this study. This model has been discussed in our earlier papers (e.g., Knutson and Manabe 1995, and references therein). As we will show in this report, the higher-resolution (R30) model appears to give a more realistic simulation of internal climate variability; however, the R15 model results are used here for specific purposes where a comparable R30 model simulation is not yet available. For example, a 2000-yr control integration (with no change in external forcing) is available for the low-resolution model. This long simulation of internal variability is important for our assessment of the observed multidecadal to century-scale SST changes, since a simulation of many centuries is important for such an analysis. The remaining two low-resolution experiments are simulations (from slightly different initial conditions) of twentieth-century climate change. These experiments use the IS92a scenario (Houghton et al. 1992) of estimated past or projected future greenhouse gas and sulfate aerosol forcing for the period 1765–2065 (Haywood et al. 1997). They are used here to assess the possible role of anthropogenic forcing in the recent Pacific SST changes. The radiative effect of all greenhouse gases is represented in terms of an equivalent CO_2 concentration, and the direct radiative sulfate aerosol forcing is parameterized in terms of specified spatially dependent surface albedo changes following Mitchell et al. (1995). A higher-resolution (e.g., R30) simulation of the CO_2 + aerosol climate changes is not yet available.

b. Observed data sources

The primary observed SST dataset used for the study is the GISST2 dataset developed at the Hadley Centre (Rayner et al. 1996). For this dataset, eigenvector re-construction techniques have been used to extend SST global coverage back to 1871; we use data from 1900 to 1994. The period prior to 1949 is particularly dependent on the reconstruction technique due to the greater amount of unavailable data, but the GISST2 reconstruction provides at least a tentative estimate of SST variations extending back over the past century. Although the GISST2 data is available on a 1° × 1° grid, the data has an effective resolution of about 4° × 4° prior to 1950 (D. E. Parker 1996, personal communication). Therefore, we have averaged the 1° data into 5° × 5° regions so that the effective spatial resolution remains roughly constant over the analysis period. We also used the Hadley Centre's Meteorological Office Historical Sea Surface Temperature version 6 dataset, updated through February 1996 (Parker et al. 1995). This dataset does not use EOF reconstruction, but provides SST anomaly estimates on a 5° × 5° grid for those locations and months where data is available. Observed sea level pressure (SLP) anomalies used in this study are from Trenberth and Paolino's (1980) Northern Hemisphere SLP dataset, updated through May 1995, available from the National Center for Atmospheric Research (NCAR) (http://www.scd.ucar.edu/dss).

c. Time filtering and trend separation

For the comparisons of model and observed variability, SST time series are first decomposed into three components: the century-scale linear trend, decadal variability, and ENSO variability. Decadal variability in our study is defined as >7-yr variability minus the century-scale linear trend. A period of 7 yr is taken as the dividing frequency (0.5 amplitude response) between ENSO and decadal variability. Further details and discussion of the time filter design is contained in the appendix. An example illustrating the relationship between the >7-yr filtered and "unfiltered" (5-month running mean) data was shown in Fig. 2. The century-scale linear trend component may contain some natural internal variability that projects onto the linear trend; alternatively, the residual decadal variability could contain an anthropogenic climate change component that has a nonlinear time dependence. These possibilities are explored in more detail in section 5.

For the model, the decadal variability was analyzed based upon detrended data from the control run rather than the +1% yr^{-1} CO_2 run since the CO_2-induced SST trend in the latter was slightly nonlinear, which would have resulted in some contamination of the *internal* variability estimate, even after removal of a linear trend.

The separation of the low-frequency (>7 yr) variability into linear trend and decadal components differs from the approach of Zhang et al. (1997), who compute low-frequency EOFs after subtracting out a "global warming mode" that they take to be a *spatially uniform* field whose value everywhere is the global mean SST anomaly. However, we present evidence elsewhere in
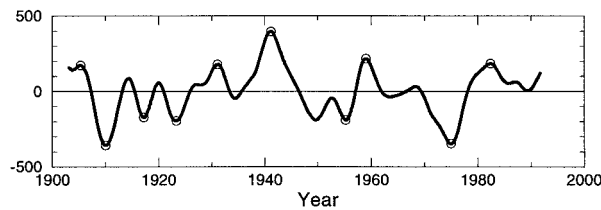
FIG. 3. Time series of the first principal component (PC1) of observed Pacific region SST based on the GISST2 reconstruction over the region 45°N–45°S. Circles denote reference dates selected for the warm (positive) and cold (negative) decadal composite phases. These dates were selected according to the following criteria: (i) PC1 exceeded one standard deviation in absolute value, and (ii) the selected date had the largest anomaly occurring between the previous and subsequent "zero-crossing" of the PC1 series. The underlying EOF1 was computed from the detrended low-pass filtered (>7 yr) data using the correlation matrix method; the results presented are based on unrotated EOF1.

this study that the simulated response to increased CO_2 in the Pacific region is not spatially uniform but appears to have a pattern with some similarity to the model's internal decadal variability. By first removing a separate linear trend at each grid point, we retain the spatial structure of the linear trend field for comparison to the model-simulated trend.

3. Decadal and ENSO variability

a. Decadal variability: Observed versus simulated

We begin by describing the decadal variability composites for the observed (GISST2) and R30 model data. The first principal component (PC1) of the GISST2 data for the Pacific region (45°N–45°S) is shown in Fig. 3. Based on this curve, five warm and five cold events (circles) were selected as reference dates for constructing composite warm and cold events (see caption). Using >7-yr filtered data for these dates, a composite "event" (warm phase minus cold phase) for the observed decadal variability is presented in Fig. 4b. Thus Fig. 4b illustrates the trough-to-peak change in SST between the cold and warm phases of a composite decadal variability episode.

The observed decadal composite in Fig. 4b shows a triangular-shaped warm anomaly region extending from the west coasts of North and South America in the subtropics westward to a region near the date line along the equator. These pronounced warm anomalies display considerable symmetry about the equator. In the Northern Hemisphere the warm anomalies extend poleward along the west coast of North America, reaching the Gulf of Alaska. The warm anomalies are flanked, in the central and western parts of the Pacific basin, by negative (cool) anomalies in the subtropical to middle latitudes of both hemispheres. The cool anomalies appear slightly stronger in the Northern Hemisphere than in the Southern Hemisphere.

Although the features mentioned above are not all present in each of the individual events used to construct the composites (not shown), the composites appear to provide a reasonable representation of the "typical" event. A local two-sided t test was done for the warm and cold composite anomaly fields separately, assuming the warm dates were temporally independent and the cold dates were temporally independent. According to this test, the anomalies were generally significant to at least the 0.1 level over most of the triangular Pacific region (both warm and cool tropical phases). As for the negatively correlated anomalies in the extratropical North Pacific, the anomalies over much of this region were significant (0.1 level) for the warm Tropics/cool extratropics phase, but only a small part of the region had significant anomalies for the opposite (cool Tropics/warm extratropics) phase. The extratropical central Pacific anomalies are approximately a factor of 2 larger in the warm Tropics/cool extratropics phase than in the opposite phase.

The R30 model's decadal composite (Fig. 4e) shows considerable similarity to the observed decadal composite (Fig. 4b) in terms of its amplitude and pattern. The correlation coefficient between the two fields over the Pacific domain 45°N–45°S, hereafter denoted by r_{xy}, was 0.75. Of particular note is the triangular-shaped warm anomaly pattern in the Tropics, with the warm anomalies extending northward along the North American coast to the Gulf of Alaska, and the accompanying cold anomalies in the subtropical to middle latitudes of both hemispheres. The chief discrepancy appears to be the overly intense warm anomalies just west of the date line in the model; in addition, the model's extratropical cool anomalies appear somewhat more intense than their observed counterparts. A map of the composite decadal variability for the lower-resolution (R15) model (not shown) has substantially weaker anomalies than the R30 or observed composites in Figs. 4b and 4e, although the pattern is similar. The decadal composites (R30 model or observed) are also both similar to the recent (1949–94) trend pattern in Fig. 1, with r_{xy} of 0.61 and 0.76, respectively. Although not shown here, during the simulated warm tropical SST phase, substantial positive precipitation anomalies (i.e., positive tropospheric condensation heating anomalies) are simulated in the western equatorial Pacific region.

Observed and simulated SLP and SST anomalies over the extratropical North Pacific and North America region are shown in Fig. 5. These are constructed for the warm tropical/cool extratropical phase of the decadal variability. The agreement between simulated and observed anomalies is fairly good, with negative SLP anomalies in the region indicating that a strengthening of the Aleutian low accompanied the pronounced cool SST anomalies near 40°N. In both the observed and simulated composites, the strengthened Aleutian low, the weaker high SLP anomalies over North America and the low SLP anomalies near the east coast of North America yield an overall pattern reminiscent of the Pa-
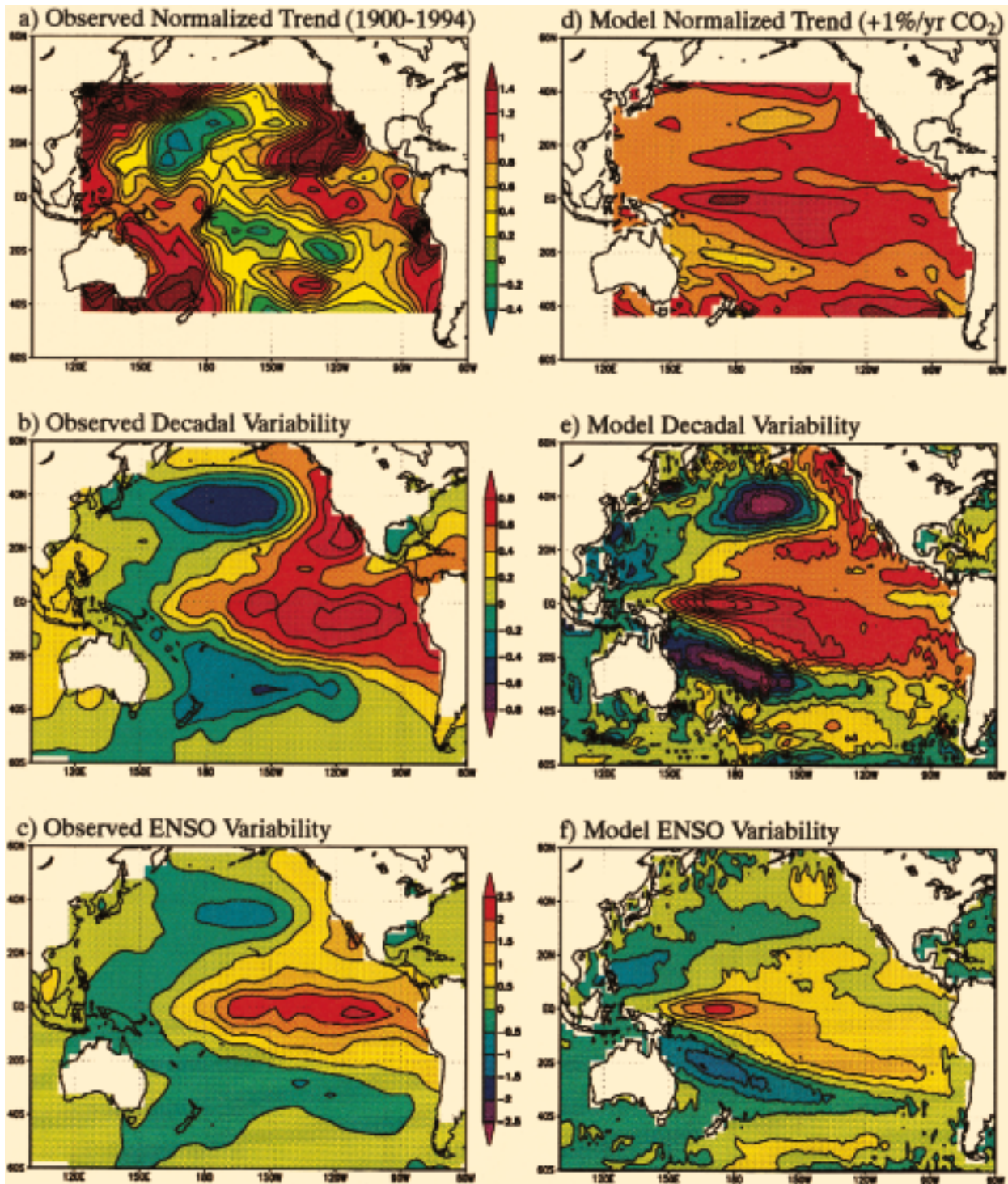
FIG. 4. (a) Linear trend in observed Pacific SST (1900–94, GISST2 5° × 5° dataset) divided by the linear trend in global SST over the same period of 0.74°C (100 yr)$^{-1}$. Contour interval of 0.2. (b) Observed decadal timescale (>7 yr, detrended) SST composite (warm minus cold) for the years 1900–94. Contour interval of 0.2°C. (c) Observed ENSO timescale (<7 yr) SST composite (warm minus cold). Contour interval of 0.5°C. (d) Simulated CO_2-induced linear trends based on years 21–120 of two R30 coupled model experiments. The net trend (i.e., the trend from the +1% yr^{-1} CO_2 experiment minus the trend from the control experiment) is shown to account for a relatively small trend in the control run. Contour interval of 0.2. (e) As in (b) but based on years 21–120 of the R30 coupled model control experiment with four warm and four cold phase dates included in the composites. (f) As in (c) but based on years 21–120 of the R30 coupled model control experiment. The color scale between each pair of maps [e.g., (a) and (d)] indicates the shading convention used for the pair of maps. The shaded regions on the maps in (a) and (d) illustrate the domain used for the EOF analyses in this study. See text and Fig. 3 caption for compositing method.
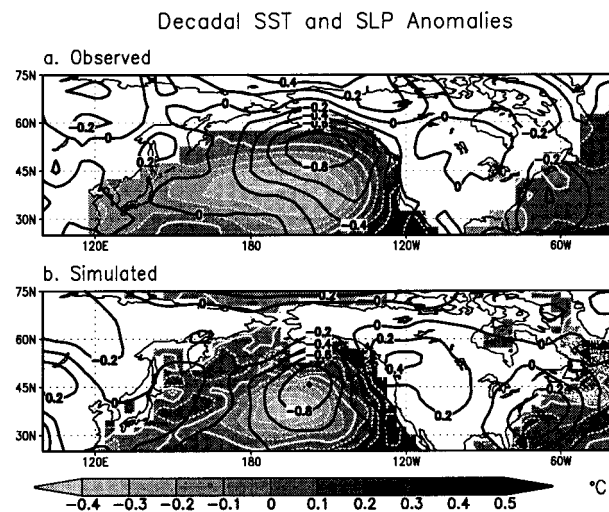
Decadal SST and SLP Anomalies

FIG. 5. Composite decadal SST (shading, white contours) and sea level pressure (SLP, dark contours) anomalies over the extratropical north Pacific and North America for the warm tropical/cool extratropical phase of decadal variability. Results are shown for (a) observations and (b) the R30 coupled model. Due to missing data periods, the observed SLP composite is based on *5-yr means* of all available data centered on the selected composite dates, rather than on the low-pass filter described in the appendix. Note that these composites are constructed using only the warm tropical/cool extratropical phase of the decadal variability (rather than warm minus cold phases, as in Fig. 4). Thus, the dates used for the observed composites were the five positive circled dates in Fig. 3. For the R30 coupled model, >7-yr filtered data are used for both SST and SLP. The contour interval is 0.1°C for SST and 0.1 mb for SLP. The solid white contour is the zero contour for SST.

cific–North American (PNA) pattern described by Wallace and Gutzler (1981) and others (see also Zhang et al. 1997). Note that the cool SST anomalies in the North Pacific are located in regions of northerly or northwesterly surface wind anomalies, as inferred from the superimposed SLP contours, whereas the warm SST anomalies near the west coast of North America occur in regions of southerly surface wind anomalies. The particular model processes that produce these extratropical SST anomalies will be examined later in this section.

b. ENSO variability: Observed versus simulated

The observed ENSO (<7-yr timescale) composite is shown in Fig. 4c. The composite anomalies (warm minus cold), were constructed based on 18 warm and 18 cold events in the years 1900–94. The 1990s ''warm event'' was not included in the ENSO composite, as it projected mainly onto the decadal data. The observed ENSO variability pattern in Fig. 4c appears considerably more enhanced in the equatorial region than does the observed decadal variability pattern (Fig. 4b). This difference in meridional scale has been noted previously, for example, by Zhang et al. (1997) and Kachi and Nitta (1997). The subtropical to midlatitude cool anomalies

are much weaker, relative to the magnitude of the tropical warm anomalies for the ENSO timescale (Fig. 4c) than they are for the decadal timescale (Fig. 4b). Similarly, the warm anomalies along the west coast of North America are much less pronounced on the ENSO timescale than on the decadal timescale.

The R30 model's simulated ENSO variability (Fig. 4f) is generally much weaker than the observed ENSO variability (Fig. 4c), especially in the eastern equatorial Pacific. The simulated ENSO variability maximum (warm minus cold) of about 2°C is located near the date line. In the observed composite, the 2°C (warm minus cold) anomalies extend across the equatorial Pacific from about 170° to 90°W near the coast of South America. An apparent displacement of the maximum interannual SST variability into the western Pacific also has been noted for the NCAR coupled model by Meehl and Arblaster (1998). We speculate that our model's bias toward greater variability than observed near the date line (for both ENSO and decadal timescales) results from shortcomings in the simulation of the time-mean tropical Pacific SST and thermocline structure. These problems include a cold tongue that extends too far to the west (not shown) thus displacing the region of maximum zonal equatorial SST gradients westward toward the date line in the model. These shortcomings of the simulated time-mean state occur despite the use of flux adjustment in the model and are the subject of continued investigation.

In spite of the shortcomings in the simulated ENSO variability pattern, many features of the observed ENSO variability pattern (Fig. 4c) are reproduced by the model (Fig. 4f). For example, in both model and observations, the positive ENSO composite anomalies form a similar broad, triangular, equatorially centered pattern flanked by weak cooling in the extratropics of both hemispheres. In addition, for both model and observations, the Northern Hemisphere extratropical cooling anomaly is much weaker (relative to the tropical anomalies) for the ENSO timescale than for the decadal timescale (i.e., compare Figs. 4f and 4e and Figs. 4c and 4b). The correlation between the observed and model ENSO composites, r_{xy}, was 0.65. The ENSO variability and decadal variability patterns are quite similar to each other for both the model (Fig. 4e vs 4f, r_{xy} = 0.88) and the observations (Figs. 4b and 4c, r_{xy} = 0.91).

c. Mechanism of simulated decadal variability

Given that the simulated and observed decadal SST variability patterns and amplitudes in Fig. 4 are similar, we assume that the model can provide insight into the mechanism of the observed decadal variability. Therefore, in this section, we explore the mechanism of the model's decadal variability with the aid of model datasets (such as century-long records of subsurface ocean temperatures), which are currently not available in the observational record. While the focus of our study is

on decadal variability, we first present some model re-sults for the ENSO timescale to use as a basis for com-parison to the decadal-scale results.

For the ENSO timescale, several studies have shown how the subsurface ocean anomalies evolve during ENSO to provide the long-term memory of the phe-nomenon (e.g., Schopf and Suarez 1988, 1990; Graham and White 1988; Battisti and Hirst 1989; Cane et al. 1990; Chao and Philander 1993; Schneider et al. 1995; Kirtman 1997). With this mechanism, often referred to as the ''delayed oscillator'' mechanism, warm SST anomalies in the central and eastern Pacific induce sur-face wind anomalies that gradually cause the thermo-cline in the west to become elevated. These induced thermocline perturbations in the west eventually prog-ress eastward along the equator, elevating the thermo-cline in the eastern Pacific, initiating the cold (La Niña) phase of ENSO, and so on.

In an earlier study (Knutson et al. 1997), we showed that a similar mechanism appears to operate in our low-resolution (R15) coupled model on the ENSO timescale.

Here, an abbreviated version of the ENSO (<7 yr) timescale heat content life cycle from the R30 coupled model is presented. In Figs. 6a–f the composite ocean heat content (69–237 m) and surface wind anomalies for the simulated ENSO composites (warm minus cold phase, based on EOF1 of the SSTs) at various time lags represent approximately one-half of a life cycle. The remainder of the life cycle can be inferred from these panels by reversing the signs of the anomalies. The corresponding SST anomaly pattern for zero lag (b) is shown in Fig. 4f. The peak warm SST anomalies in Fig. 4f are accompanied by westerly wind anomalies along the equator in the western Pacific (Fig. 6b, 0 lag) and by off-equatorial windstress curl anomalies, which act to induce negative heat content anomalies (elevated thermocline) off-equator in the far western Pacific (Figs. 6a,b; −4 months to 0 lag). Meanwhile, positive heat content anomalies (deep thermocline) are centered on the equator in the central to eastern Pacific. In the re-mainder of the half life cycle shown, the elevated ther-mocline anomalies in the western Pacific merge onto
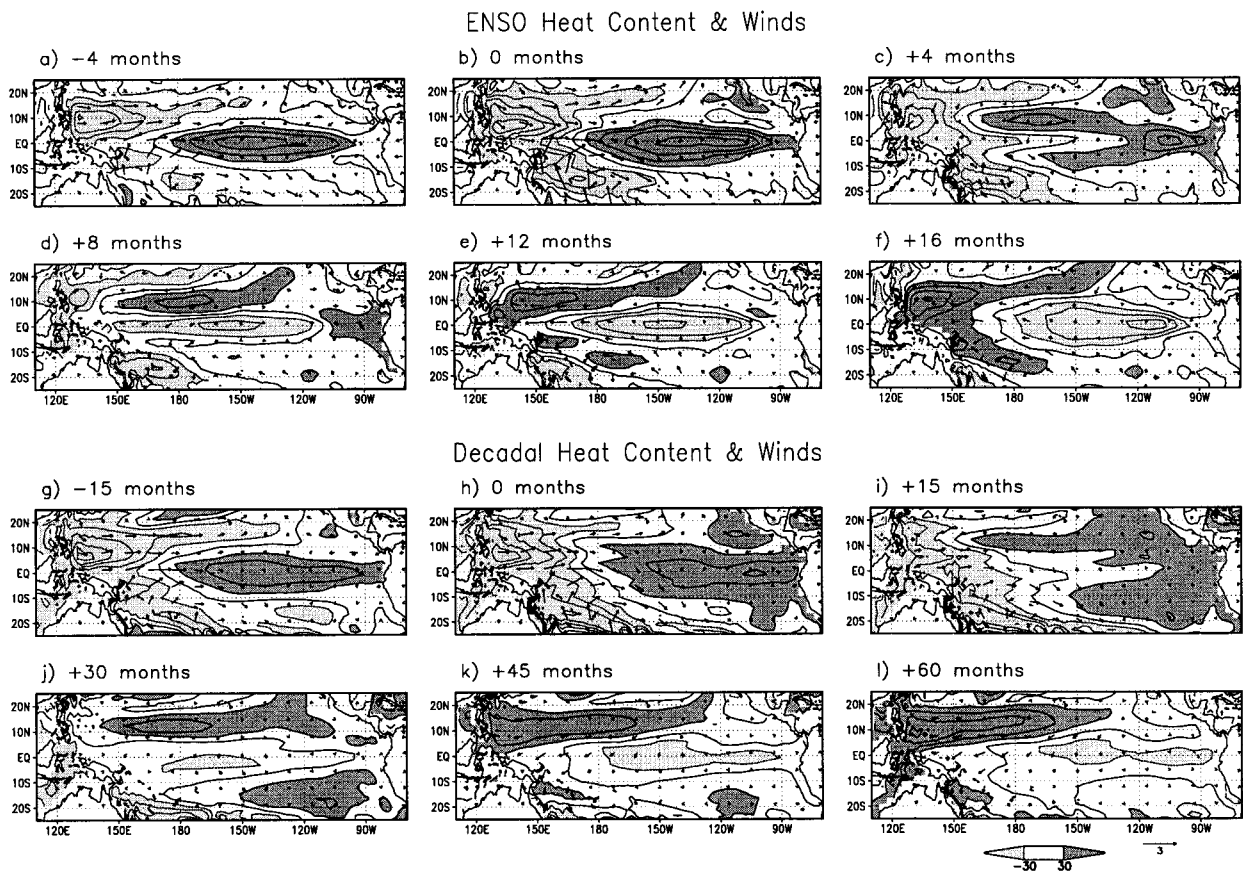

FIG. 6. Time-lagged composite ocean heat content and surface wind anomalies for the ENSO (a)–(f) and decadal (g)–(l) timescales from the R30 coupled model control experiment. The sequences of maps [(a)–(f) and (g)–(l)] depict approximately one-half of a life cycle of the composite anomalies associated with the decadal and ENSO SST variability shown in Figs. 4e and 4f. The ocean heat content anomalies are defined as the vertically integrated temperature anomaly over model layers 3–5 (69–237 m), with a contour interval of 30°C m. Values less than −30 and greater than +30 are depicted by light and dark shading, respectively. For the surface wind anomalies, a reference vector of 3 m s^{-1} is shown at the bottom of the diagram. Compositing dates were selected based on the first EOF of Pacific SST as in Fig. 4.
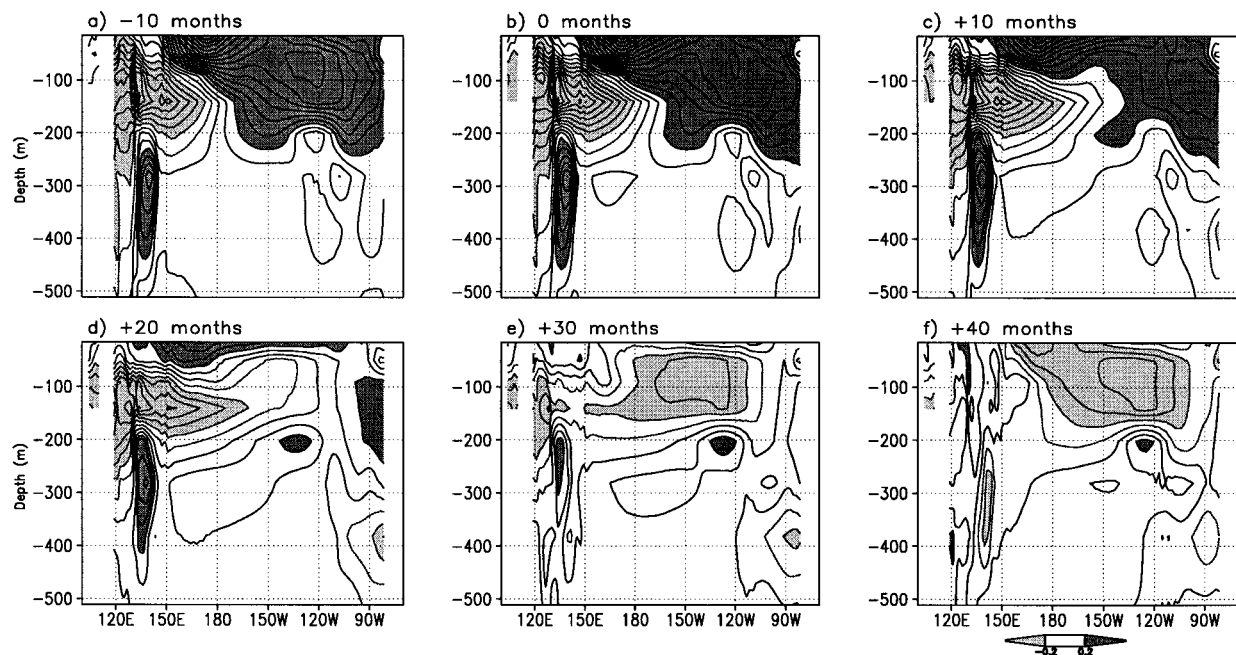
FIG. 7. Longitude vs depth cross sections along the equator of decadal ocean temperature composites (time lagged) from the R30 coupled model. (See caption for Figs. 6g–l for further details. Note that the lags shown in Figs. 6g–l differ slightly from those presented in Fig. 7.) The contour interval is 0.1°C.

the equator, and an eastward phase progression can be traced along the equator to the central and eastern Pacific (Figs. 6c–e; lags +4 to +12 months). As the eastward progressing elevated thermocline anomalies reach the eastern equatorial Pacific, the model SSTs begin entering a cooling phase (i.e., the La Niña phase of the ENSO life cycle), inducing wind stress anomalies that lead to an anomalously deep thermocline in the west, and so on. In Figs. 6c–f (lags +4 to +16 months), a westward off-equatorial phase progression of heat content anomalies from the central to western Pacific is apparent near 9°N. In situ strengthening of these anomalies occurs in the extreme western Pacific (e.g., Fig. 6f). Much of the large-scale structure in the model's composite wind anomalies is also seen in Rasmusson and Carpenter's (1982) observed ENSO wind composites (e.g., see their transition and mature phase composites). However, certain features of their observed wind composites, such as strong northerly wind anomalies over the northern tropical Pacific, are not as evident in the model ENSO simulation.

The simulated heat content and winds life cycle for the decadal (>7 yr) timescale is shown in (Figs. 6g–l). Note that the time lag in months between the individual panels in the decadal life cycle is 15 months compared with 4 months for the ENSO life cycle discussed above. The decadal life cycle shows a broadly similar pattern (and roughly comparable magnitude) to the ENSO life cycle discussed above. For example, on both timescales, the heat content anomalies just prior to the time of maximum equatorial SST warming (Figs. 6a and 6g) show

a characteristic pattern of two off-equatorial heat content anomaly regions in the western Pacific and a single equatorially centered positive heat content anomaly pattern in the eastern Pacific. A closer inspection of the life cycles indicates that the westward progressing off-equatorial heat content anomalies are centered at a slightly higher latitude (~12° vs 9°N) for the decadal timescale than for the ENSO timescale. Also the equatorially centered heat content anomalies in the eastern Pacific tend to be less intense (relative to the western Pacific anomalies) on the decadal timescale as compared to the ENSO timescale.

Figure 7 shows a longitude versus depth view of the decadal ocean temperature anomalies along the equator. Near the time of maximum SST (Figs. 7a,b; lag −10 to 0 months), cool anomalies are found in the subsurface western equatorial Pacific at ~70–200-m depth. Warm anomalies dominate the near-surface layers over most of the equatorial Pacific. In next three panels (Figs. 7c–e; lags +10 to +30 months) the cool subsurface anomalies in the west show a phase progression eastward into the east central Pacific and upward to the surface near 160°–130°W. Subsequently, the anomalies in the surface layer intensify near the date line to produce the SST pattern seen in Fig. 4e. A similar subsurface temperature evolution has been shown for the ENSO timescale (using the R15 coupled model) by Knutson et al. (1997). In terms of equatorial SST (depicted by the top level shown in Fig. 7) the composite life cycle shows mainly a standing pattern, in contrast to the propagating features appearing in the subsurface levels.

The resemblance of the simulated and observed de-cadal composites shown in Figs. 4–7 to their counter-parts for the ENSO timescale suggests that a substan-tially similar delayed oscillator mechanism is involved for both timescales in the model. The main difference between the ENSO and decadal variability patterns ap-pears to be the slightly wider meridional structure of the heat content anomalies for the decadal scale. In par-ticular, the westward off-equatorial heat content phase progression occurs at a slightly higher latitude (and with a slower apparent phase speed) for the decadal com-posite. The slower apparent westward phase progression may be related in part to the decrease with latitude of the speed of free Rossby waves (e.g., McCreary 1983; Schopf and Suarez 1990). More specifically, Kirtman (1997) has used a simple coupled model to diagnose in more detail how a broader meridional structure for the off-equatorial wind stress forcing and thermocline anomalies can lead to a longer period for ENSO-like oscillations via the effects of a stream of forced off-equatorial Rossby waves. Upon modifying the meridi-onal profile of the wind stress in his model such that the latitude of the maximum thermocline perturbations in the western Pacific increased from 8°S to 12°S, the period of the model's oscillation increased from 5 to 9 yr. The mechanisms described by Kirtman may provide at least a partial explanation for how the wider merid-ional structure of our heat content anomalies leads to the longer timescale of our model's decadal ''oscilla-tion.'' However, while there is some evidence for a wid-er meridional scale for both heat content and wind stress curl anomalies (not shown) in our coupled model on the decadal scale, it is not yet clear what mechanism leads to the wider meridional extent of these anomalies. Our present assessment of the model's decadal variability mechanism is based on the composite life cycle results described above; a more definitive determination of the mechanism would likely require specialized model ex-periments (e.g., Schneider et al. 1995) beyond the scope of the present study.

The processes in our model producing the cooling anomalies in the extratropical North Pacific during the decadal tropical warm phase are examined in Fig. 8. This figure shows a surface-layer heat budget analysis for approximately the time of maximum *cooling ten-dency* (35 months prior to the time of warmest tropical/ coolest extratropical anomalies) in the region. The net heating anomaly field (Fig. 8a) shows a broad area of net cooling centered near 40°N, 170°W and areas of net warming along the west coast of North America. Al-though the SLP anomalies at this stage of the life cycle (not shown) are much weaker than at the time of max-imum SST anomalies (Fig. 5b), the surface wind anom-aly vectors in Fig. 8a indicate anomalous northerly flow in the cooling region and anomalous southerly flow in the warming region. The net heating anomaly field is partitioned into downward surface heat flux anomalies and heating due to ocean dynamics (advection and dif-
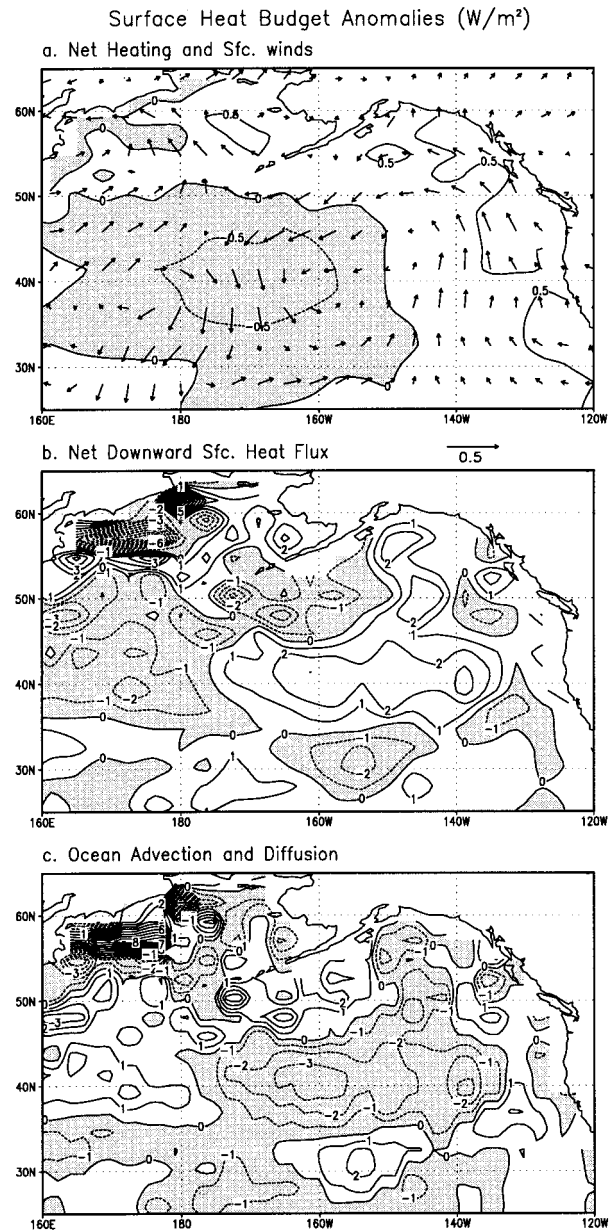

FIG. 8. Simulated decadal surface-layer heat budget composite analysis for the northern extratropical Pacific. The composites are shown for the time 35 months prior to the time of coolest extratropical (warmest tropical) SST anomalies (e.g., Fig. 4b), which is approxi-mately the time of maximum *cooling tendency* in this region; units are W m^{-2}. (a) Net heating rate (shading) and surface wind vector anomalies (arrows with a reference vector shown of 0.5 m s^{-1}). (b) Net downward surface heat flux anomaly. (c) Net heating anomaly due to ocean advection and diffusion, computed as the residual of the net heating anomaly (a) minus the net surface heat flux anomaly (b). Note the smaller contour interval in (a) (0.5 W m^{-2}) vs (b) and (c) (1 W m^{-2}).

fusive processes) in Figs. 8b and 8c, respectively. This partitioning shows that the net heating anomalies are relatively small in comparison to both the surface heat flux and ocean dynamics anomaly terms. Ocean dynam-

ics provides for the cooling tendency over much of the main cooling region (i.e., along 40°N to the east of about 175°W), while the surface heat flux contribute a net *warming* tendency. The fact that surface heat fluxes act in opposition to the net cooling tendency on the decadal scale is quite distinct from the surface budget for the ENSO timescale (not shown). On the ENSO timescale in the model, latent and sensible heat fluxes provide the dominant cooling mechanism, whereas advection effects are relatively minor. This is in agreement with diagnostic simulations of North Pacific SST anomalies associated with observed tropical SST anomalies during ENSO (Alexander 1990; Lau and Nath 1996). The more important role for ocean dynamics on the decadal timescale indicated by our results is reminiscent of the diagnostic modeling study of North Pacific interdecadal variability by Miller et al. (1994). In the region of net warming near the coast of North America, the surface heat balance patterns are more complex, with both surface heat flux anomalies and ocean dynamics playing important roles in the model.

The positive downward surface heat flux anomalies (i.e., warming tendency) in the region of maximum dynamical cooling appear to be due primarily to decreases in the air–sea temperature difference (not shown). The reduction in the air–sea temperature difference arises in the region of southerly wind anomalies (near 140°W) due to the advection of warmer air into the region. On the other hand, in the region of northerly wind anomalies (near 170°W) the reduction arises as the local SST cool anomaly is more pronounced than the overlying air temperature cool anomaly. In either case, the reduced air–sea temperature difference leads to a reduction in evaporative and sensible heat fluxes and hence to a net positive heating anomaly for the ocean surface layer. The surface wind speeds are actually slightly enhanced in the cooling region, which by itself leads to a cooling tendency in the surface heat fluxes, but this effect is more than offset by the reduced air–sea temperature difference.

Whereas the ocean dynamics contribution shown in Fig. 8c was computed as a residual from the net heating and net surface heat flux terms, the approximate contributions from ocean advection were also computed directly based upon monthly mean temperature and circulation data from the model (not shown). These results indicate that ocean advection (as opposed to diffusive processes) is the dominant source of the cooling tendency in the main cooling region. An examination of the individual ocean temperature advection terms indicates that zonal, meridional, and vertical advection terms all make substantial contributions to this cooling tendency. As one example, anomalous southward ocean surface currents in the region of northerly wind anomalies advect cooler waters southward.

We speculate that the ocean circulation changes in the model that produce the advective cooling on the decadal timescale are induced by overlying atmospheric wind anomalies. Presumably, the strengthened Aleutian low is a response to the tropical SST and condensation heating anomalies (not shown) associated with the tropical warm SST phase. However, to demonstrate this chain of causality conclusively would require additional experiments beyond the scope of this study. In any case, our composite results demonstrate that the processes by which the extratropical ocean cooling occurs differ substantially for the ENSO and decadal timescales, with ocean circulation anomalies in the near-surface layer becoming relatively more important on the longer (decadal) timescale.

The tropical–extratropical decadal variability described in Figs. 4–8 appears to relate to the observed variability described by Trenberth (1990), Trenberth and Hurrell (1994), Deser and Blackmon (1995, their EOF1), and Zhang et al. (1997), with a strong tropical component and pronounced tropical–extratropical SST connection. It also resembles the decadal variability recently simulated by Yukimoto et al. (1996) using a coupled model at the Meteorological Research Institute of Japan. On the other hand, the simulated North Pacific decadal variability in the present study does not appear to depend on the subtropical gyre mechanism proposed by Latif and Barnett (1996). While Latif and Barnett comment that the Tropics play only a minor role in the simulated decadal variability they analyze, the Tropics appear to play a crucial role in our simulated decadal phenomenon. Although they analyze a different EOF domain (northern Pacific only), which makes direct comparison difficult, the decadal variability they discuss may be more closely related to Deser and Blackmon's EOF2, which is primarily an extratropical North Pacific mode. Although not shown here, the second EOF in our R30 coupled model's North Pacific (T. Delworth 1996, personal communication) describes variability similar to Deser and Blackmon's EOF2. This extratropical Pacific variability is the subject of a separate study. Recently, Gu and Philander (1997) have proposed a theory for decadal climate variability in the Pacific involving the propagation of subsurface temperature anomalies along constant density surfaces between the extratropical Pacific and the equatorial thermocline. Our examination of composite decadal subsurface temperature anomalies in the midlatitudes in our model reveals some evidence for subsurface propagating features similar those described for the North Pacific by Deser et al. (1996, their Fig. 10). However, in our model the anomalies do not appear to propagate to the equatorial thermocline region to initiate the subsequent event, and thus Gu and Philander's mechanism does not appear to be responsible for the decadal-scale variability simulated in our study.

4. Simulated versus observed trend patterns

a. Observed linear trends

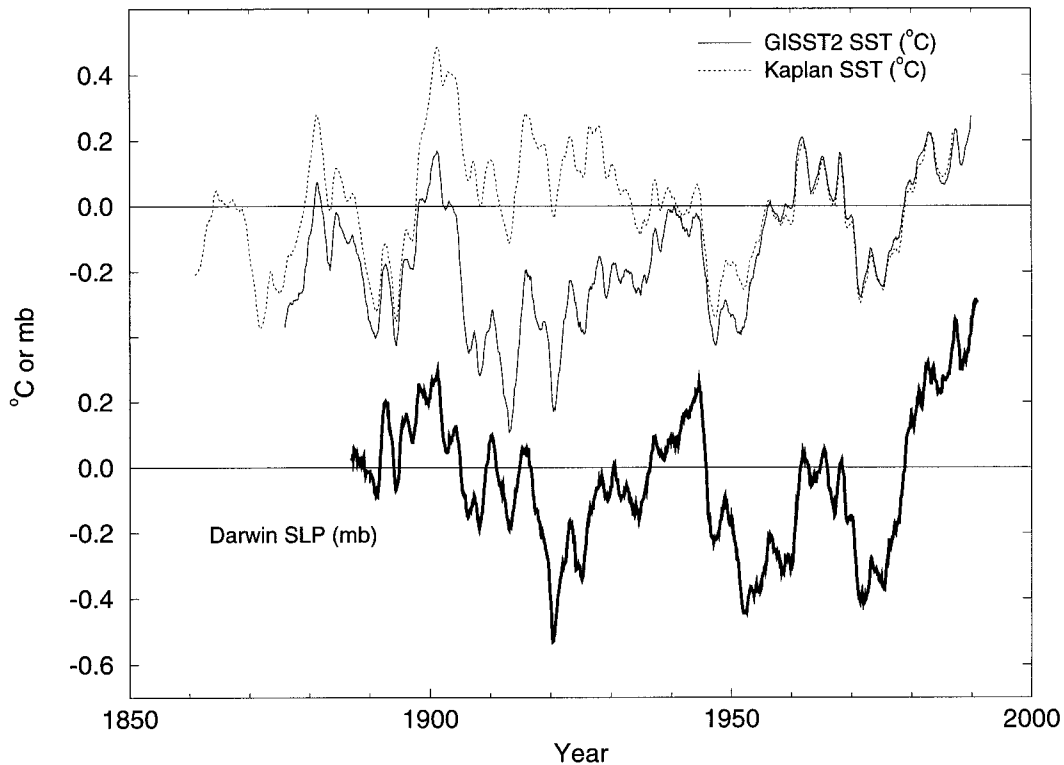The observed linear trend for a period of relatively reliable SST records (1949–94) was shown in Fig. 1

FIG. 9. (Top) SST anomalies for the NINO3.4 region (5°N–5°S, 170°–120°W) from the GISST2 and Kaplan et al. (1997) SST data reconstructions (see legend). (Bottom) Darwin SLP anomalies in mb. All anomalies are relative to a 1961–90 base period and are presented as 10-yr running means in order to highlight very low frequency variability and trends.

and discussed briefly in the introduction. Figure 4a shows the linear trend for the period 1900–94 based on the GISST2 SST reconstruction. For the purposes of comparison to the model CO_2-induced trend later in this section, the observed trend at each grid point in Fig. 4a has been normalized by dividing by the trend in the global average SST over the period. Thus, areas with red shading (>1.0) indicate regions where the linear trend exceeds that of the global mean SST, whereas dark green and blue areas indicate regions of negative (cooling) trends. Positive (warming) trends occur over most of the domain, with a relatively small cooling trend in two regions reminiscent of the cooling regions of the decadal variability pattern. Large regions of the eastern Pacific basin show warming in excess of the global average, which, along with a region near the equatorial date line region, form a triangular-shaped region reminiscent of the observed decadal variability pattern discussed in the previous section. However, the overall correlation, r_{xy}, between the observed 1900–94 trend field and the observed decadal variability composite (Figs. 4a and 4b) was only 0.14.

Recently Cane et al. (1997) presented a linear trend (1900–91) map for the Pacific that has some broad features in common with that in Fig. 4a, but with some substantial differences as well. One example of a dif-

ference of particular relevance to the present study is the pronounced negative (cooling) trend [~ -0.8°C (100 yr)$^{-1}$] emphasized by Cane et al., which is centered near 0°, 140°W. No century-scale cooling trend appears in this region according to the GISST2 reconstruction (Fig. 4a). The trends shown by Cane et al. are based on a different SST reconstruction technique (Kaplan et al. 1997), which uses as input an earlier version of the Hadley Centre SST data (MOHSST5). The differences between the trend map of Cane et al. and that in Fig. 4a imply that the method of SST reconstruction can have a large impact on the regional structures in century-scale SST trend fields.

To examine the issue of long term trends in the equatorial Pacific in more detail, we show in Fig. 9 (top portion of graph) a comparison of the SST anomaly time series for the NINO3.4 region from both the GISST2 and Kaplan et al. reconstructions. The two time series show good agreement after about the mid-1950s, while the agreement is rather poor for 1900–40, with the Kaplan series systematically higher than the GISST2 series, at times by more than 0.5°C. The century-scale cooling trend in the Cane et al. analysis is seen to arise due to the pronounced warm anomalies in the first half of the twentieth century in the Kaplan reconstruction. We note that this is a period during which data were particularly

sparse in the equatorial Pacific. There is no evidence for an equatorial Pacific cooling during the relatively well-sampled post-1950 period in either dataset, which supports the 1949–94 trend results presented in Fig. 1. To gain some additional perspective on the pre-1950 SST anomalies, we show in Fig. 9 (bottom portion of graph) a time series of Darwin SLP anomalies, which is used as an independent proxy measure of the zonal SST gradient in the equatorial Pacific. We speculate that if a regional equatorial SST cooling trend (i.e., intensification of the cold tongue) had occurred in the period 1900–50, the Walker circulation would have intensified, which should have been reflected in an upward trend in the SOI and possibly a downward trend in Darwin SLP. (Note that the fluctuations in the Darwin SLP series track the SST anomaly fluctuations reasonably well in the post-1950 period.) In the period 1920–45 the Darwin SLP record shows a fairly continuous rise, which seems consistent with the GISST2 record but not with the Kaplan record, which shows a decrease over the same time period. The very low SST anomalies around 1912 in the GISST2 record do not seem as consistent with the Darwin record as most of the other major fluctuations. Overall, the Darwin record from 1900 to 1950 appears more consistent with the GISST2 SST reconstruction than with Kaplan reconstruction. In particular, the Darwin SLP data does not appear to support the notion of a pronounced regional equatorial Pacific cooling trend during the first half of the twentieth century. This preliminary assessment is just one approach for examining the issue of equatorial Pacific SST trends, but based on the results presented here, we have chosen to rely on the GISST2 reconstruction for the century-scale trend estimate in Fig. 4a. Nonetheless, the issue of the reliability and relative merit of different SST reconstructions remains unresolved at present.

b. Simulated CO_2-induced warming pattern

The normalized linear trend for the $+1\%$ yr^{-1} CO_2 experiment of the R30 coupled model is shown in Fig. 4d. The trend results shown are the *net* trend ($+1\%$ yr^{-1} CO_2 run trend minus control run trend) for years 21–120 of the experiments. The first 20 yr of both runs were skipped to reduce the effect of the slightly nonlinear trend behavior in the CO_2 increase experiment, in which the warming is relatively slow for about the first 20 yr, followed by a more constant linear trend over the remaining years (21–120). The net trend at each grid point has been normalized by the net trend in the global mean SST of 2.93°C (100 yr)$^{-1}$.

The model-simulated CO_2 warming pattern (Fig. 4d) shows the Pacific warming exceeding the global mean SST warming rate in a triangular-shaped region resembling both the region of warm anomalies for the observed 1949–94 SST trend (Fig. 1) and the simulated and observed decadal variability pattern discussed previously (Figs. 4b,e). The triangular region of enhanced

warming in Fig. 4d is flanked in both hemispheres by subtropical regions of more moderate warming (less than the global mean rate). These more slowly warming regions correspond roughly to the cool anomaly regions in the decadal variability composites (Figs. 4b,e) and Fig. 1. The correlation r_{xy} between the model's CO_2-induced warming pattern and the model's internal decadal variability pattern (Fig. 4d vs 4e) is 0.55. The correlation between the CO_2-induced warming pattern and the 1949–94 trend (Fig. 1) is 0.39. The overall correlation between the model's CO_2-induced warming pattern (Fig. 4d) and the century-scale trend pattern (Fig. 4a) is negligible ($r_{xy} = 0.02$), with the simulated CO_2-induced warming being much more spatially uniform than the observed trend pattern. However, one important aspect of agreement between these two maps is that they both indicate a positive (warming) trend over most regions of the Pacific from 45°N to 45°S. A century-scale cooling trend is indicated only in a relatively small fraction of the Pacific domain in the observations, whereas no areas of cooling are found in the Pacific (45°N–45°S) for the simulated CO_2-induced warming. The maximum CO_2-induced warming in the Tropics, exceeding the global mean by up to 40%, occurs near the equatorial date line; this is virtually the same region where the model's decadal and ENSO variability maximum was found. We note, however, that the R30 model shows a tendency to overestimate the amplitude of ENSO and decadal variability near the equatorial date line region, and thus the occurrence of pronounced CO_2-induced warming in date line region in particular may be related to a model deficiency.

The CO_2-induced warming response of the R30 coupled model can be compared to that of the lower-resolution (R15) model discussed in Knutson and Manabe (1995, Figs. 3 and 6). A decade-by-decade inspection of the R30 model's CO_2-minus-control anomalies (not shown) indicates that the pattern in Fig. 4d is present in all decades beyond about year 50. Thus this pattern is evident much earlier in the integration than the reduced zonal SST gradient pattern in the R15 coupled integration of Knutson and Manabe (1995), in which the reduced SST gradient was not clearly apparent for the entire first century of integration. The long (~100 yr) "delay" in the appearance of the nonuniform pattern in the Knutson and Manabe (1995) study may have been partially due to a masking of the signal by multidecadal variability. In any case, the earlier appearance of the pronounced nonuniform Pacific warming pattern in the R30 model, compared to the R15 model, is in closer agreement with the coupled model result of Meehl and Washington (1996), who found a noticeable reduction of the equatorial Pacific zonal SST gradient within the first few decades of their transient CO_2 experiment. Another distinction between the R30 and R15 model results is that the pattern of warming in the R30 model (Fig. 4d), with an enhanced warming in a broad triangular region and less warming in regions of the subtropical

Pacific, bears a somewhat greater resemblance to the recent observed trend pattern (Fig. 1, $r_{xy} = 0.39$) than does the much more uniform warming pattern from the first 120 yr of the R15 model +1% yr^{-1} CO_2 experiment (not shown).

One can speculate that the observed century-scale trend pattern in Fig. 4a could have resulted from a combination of a gradual, relatively uniform CO_2-induced warming trend and a pronounced natural decadal or multidecadal warm episode near the end of the record (i.e., after the mid-1970s). For example, the pattern in Fig. 4a shows positive values (warming) in most regions, reminiscent of the R30 model's CO_2-induced warming pattern (Fig. 4d). Many of the remaining features in the observed trend field are reminiscent of features in the simulated and observed decadal variability patterns (Figs. 4b and 4e). However, this interpretation does not help explain certain other features, such as the strong warming trends in the far northwestern and southwestern parts of the domain in Fig. 4a.

c. Mechanism and discussion of CO_2-induced warming

In this section, we attempt to provide some insight into the mechanism producing the distinct CO_2 warming pattern in the R30 coupled model (Fig. 4d). First, the coupled model pattern is compared with the pattern of CO_2-induced warming from an R30 *mixed layer* model experiment with the same atmospheric GCM component (Wetherald 1996). The mixed layer model uses a heat flux adjustment technique to ensure a realistic SST simulation for the model control climate. The heat flux adjustments are added to the model-computed surface heat flux into the (50 m) mixed layer in order to maintain a realistic seasonal cycle of SST in the model. Thus, they primarily "correct" for the obvious lack of ocean heat transport in the mixed layer model and also for the net effect on SST of various other deficiencies in the model. In the 2 × CO_2 equilibrium experiment, the same heat flux adjustments are used as in the control (1 × CO_2) mixed layer experiment, with the underlying assumption being that the horizontal heat transport by ocean currents remains invariant with increasing CO_2. We can infer that features in the coupled model response that do not appear in the mixed layer model are dependent on interactive ocean dynamics. Conversely, common features in the coupled and mixed layer model responses do not depend crucially on interactive ocean dynamics, since that mechanism is absent in the mixed layer model.

For the coupled model, Fig. 10a shows the difference between years 81–120 of a +1% yr^{-1} CO_2 transient run and years 81–120 of a control run; for the mixed layer model (Fig. 10b), the difference between a 2 × CO_2 and 1 × CO_2 equilibrium experiment are shown. For both the coupled and mixed layer model results (Figs. 10a,b), the SST difference fields are normalized by di-

viding the SST change at each grid point by the global mean SST difference for the respective experiments.

We first examine the unique features in the coupled model result, which we can infer depend on interactive ocean dynamics. The most pronounced such feature is the tongue of enhanced warming in the equatorial Pacific in the coupled model (Figs. 10a and 10d). This enhanced warming appears to result from ocean circulation changes, such as the reduced equatorial ocean upwelling in the coupled model (Fig. 10c). For example, the maximum time-mean equatorial upwelling between the top two layers in the model decreases by over 20%, from 102 cm day^{-1} in years 81–120 of the control experiment to 79 cm day^{-1} in years 81–120 of the CO_2 increase experiment. The reduced upwelling apparently represents part of a coupled ocean–atmosphere response to decreased easterly surface wind stress and enhanced mean meridional surface wind convergence near the equator in that region (not shown). Associated with these changes is a CO_2-induced reduction in the model's Tahiti-minus-Darwin surface pressure difference of about 1 mb by years 81–120 of the experiments. The reduced easterly wind stress in the coupled model appears to be initiated by processes not crucially dependent on ocean dynamics, since it is already evident (not shown) along with a slightly reduced zonal equatorial SST gradient (Fig. 10d) in the R30 mixed layer experiment. The pattern of weaker easterlies and zonal SST gradient in the mixed layer model is then apparently modified (amplified) in the equatorial region by interactive ocean dynamics (e.g., reduced equatorial upwelling) in the R30 coupled model.

We next consider features that occur in both the mixed layer and coupled model responses (Figs. 10a and 10d). Both models show enhanced warming in a region extending from near the west coast of North America southwestward past Hawaii and in a second enhanced warming region near the west coast of South America. As noted above, the latter feature is much more pronounced and extends much farther west across the equatorial Pacific in the coupled model (Fig. 10a) than the mixed layer model (Fig. 10d). Both models show a region of less warming extending northeastward from the northern Philippines, and a second region of relatively less warming in the southwest Pacific, extending from the north Australia region southeastward toward Chile. Finally, a third band of less warming along ~10°N in the coupled model is not as clearly apparent in the mixed layer simulation.

While the coupled model–mixed layer model comparison can indicate where interactive ocean dynamics is an important mechanism, determining the mechanisms for other features in the simulations is very difficult without additional experiments. The reduction of the zonal equatorial SST gradient in the mixed layer experiments is consistent with the evaporative damping mechanism proposed in Knutson and Manabe (1995). There it was noted that evaporative cooling should in-
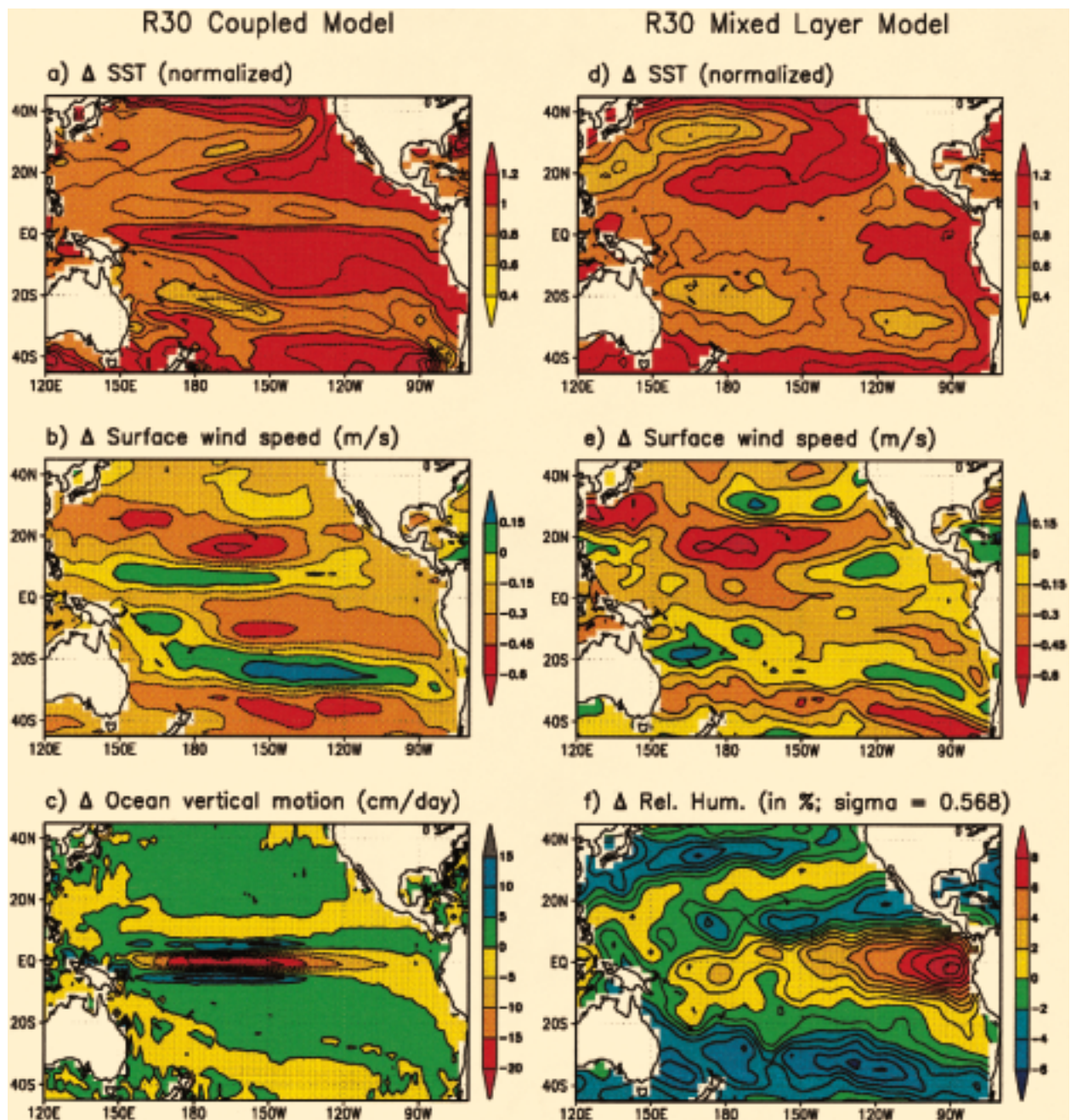
FIG. 10. CO_2-induced changes in SST (a), (d); surface wind speed (b), (e); ocean vertical motion (c); and midtropospheric relative humidity (f) from the R30 coupled model (a)–(c) or R30 mixed layer model (d)–(f). For the coupled model (a)–(c) the results shown are based on the difference between the $+1\%$ yr^{-1} CO_2 experiment (years 81–120) and the control experiment (years 81–120). For the mixed layer model (d)–(f), the results shown are based on the difference between decade-length means from $2 \times CO_2$ and $1 \times CO_2$ equilibrium experiments. The SST difference maps (a), (d) have been normalized by dividing by the global mean change in SST of 2.58°C (coupled model) or 2.55°C (mixed layer model). The ocean vertical motion is that at the interface between the top two layers of the ocean model. The surface wind speed is based on time averages of daily wind speed samples, rather than on time averages of the zonal and meridional components. The midtropospheric relative humidity is based on the model sigma surface on which the pressure is 0.568 times the surface pressure. The contour interval for (a) and (d) is 0.2; for (b) and (e) 0.15 m s^{-1}; for (c) 5 cm day^{-1}; and for (f) 1%. Note the reversal in color shading conventions for the surface wind speed [(b) and (e)] and ocean vertical motion (c) figures. For wind speeds, "warmer" colors indicate larger decreases in surface wind speeds. For ocean vertical motion (c) warmer colors indicate a sinking tendency (i.e., reduced upwelling in the equatorial region).

crease more (per degree of SST warming) in the western Pacific than in the east because of the warmer SSTs in the west (and the nonlinear dependence of saturation mixing ratios on temperature). They noted that this effect should act to reduce the SST gradient as the climate warms. As a preliminary attempt to identify mechanisms for the other features common to the mixed layer and coupled model SST response, a number of model variables were examined for evidence of a similar patterns to these SST features. One model variable with a pattern of changes resembling the SST changes is the surface wind speed field (although with the sign of the changes reversed), as is shown by comparing Figs. 10b and 10e with Figs. 10a and 10d, respectively. Apart from the equatorial date line region (discussed earlier), local maxima in SST increase tend to be accompanied by a local maxima in the *decrease* of surface wind speed. In particular, note in Fig. 10 the enhanced warming (red) and pronounced decrease in wind speeds (red) in the North Pacific near 20°N, 170°W. Since a decrease in surface wind speeds should lead to decreased evaporative cooling, this pattern is consistent with enhanced SST warming in these regions, from a surface energy balance perspective. A second variable, which may be relevant to the enhanced eastern equatorial Pacific warming, is midtropospheric relative humidity (Fig. 10f, shown for the mixed layer experiment only). Increased midtropospheric relative humidity (and decreased atmospheric subsidence) tends to occur in the eastern equatorial Pacific, accompanied by an enhanced downward flux of terrestrial radiation. This preliminary analysis suggests that several mechanisms, including spatial differences in the evaporative cooling response and midtropospheric relative humidity changes, may contribute to the SST warming pattern in the mixed layer model. The relative magnitudes of the contributions of the individual mechanisms remain to be evaluated in future studies. However, each of these mechanisms (as well as the reduced equatorial upwelling and reduced Tahiti-minus-Darwin pressure gradient in the coupled model) is consistent with an overall picture of a slight CO_2-induced decrease in the intensity of the Walker circulation and Pacific trade wind system. The weakening of the Walker circulation in response to increased CO_2 is consistent with our previous low-resolution coupled model analysis (Knutson and Manabe 1995).

The simulated response of tropical Pacific SSTs to increased greenhouse gases has been a subject of increasing interest in the climate modeling community. For example, a substantial overall warming of the tropical Pacific in response to increased CO_2 is indicated in the recent coupled model studies of Knutson and Manabe (1995), Mitchell et al. (1995), Tett (1995), and Meehl and Washington (1996). In contrast, Clement et al. (1996) have argued that the influence of ocean dynamics could actually cause eastern tropical Pacific SSTs to *cool* in response to a uniform positive heating (see also Cane et al. 1997). The Clement et al. study

was based on the response of the Cane–Zebiak model (Zebiak and Cane 1987). In that model, the temperature of equatorial upwelled water is held fixed, whereas in reality the CO_2-induced warming at higher latitudes should lead to a warmer thermocline after a delay of a few decades.

In a related study, but where the thermocline temperature was allowed to vary, Seager and Murtugudde (1997) analyzed the response of a regional (30°N–30°S) Pacific ocean GCM–atmospheric mixed layer model to a uniform surface heating. Since the winds in their model were externally specified, ocean–atmosphere coupling through wind stress feedback was not included. They found warming everywhere, although the warming of the equatorial Pacific was reduced in the presence of varying ocean heat transport (but constant winds). In contrast, in our R30 coupled model, the wind-driven equatorial upwelling is *reduced* (Fig. 10c) leading to an enhancement of the equatorial warming in the coupled model relative to our R30 mixed layer ocean experiment (Figs. 10a and 10d). We note that even neglecting ocean dynamics, the response of our R30 atmosphere–mixed-layer ocean model is quite different from the response of Seager and Murtugudde's atmospheric mixed-layer–ocean mixed layer model (compare our Fig. 10d vs their Fig. 7). This suggests that the atmospheric model components are an importance source of differences between our results and those of Seager and Murtugudde. There are many differences between our R30 atmospheric GCM and their atmospheric mixed-layer model, which could potentially be quite important in the context of climate change experiments. For example, their model uses externally specified winds, solar radiation, and cloud cover, and it does not model processes above the atmospheric mixed layer nor require the climate system to be in a state of global energy balance at the top of the atmosphere. Finally, in their experiments a spatially uniform heating perturbation is imposed, whereas the radiative forcing due to increased CO_2 is not spatially uniform but larger in the eastern Pacific than in the west (e.g., Mitchell et al. 1995). How Seager and Murtugudde's results would be affected by use of a less simplified atmospheric model component or a more spatially varying imposed heating remains to be seen.

5. Pacific triangular region indices

In the previous sections the internal decadal variability and CO_2-induced trends in the R30 coupled model Pacific region were examined and compared with observed variability. A broad triangular-shaped region of the tropical Pacific (TPAC) was identified as an important region with regard to both decadal variability and the longer-term trends. In this section, simulated and observed timeseries over the TPAC region are examined in more detail.

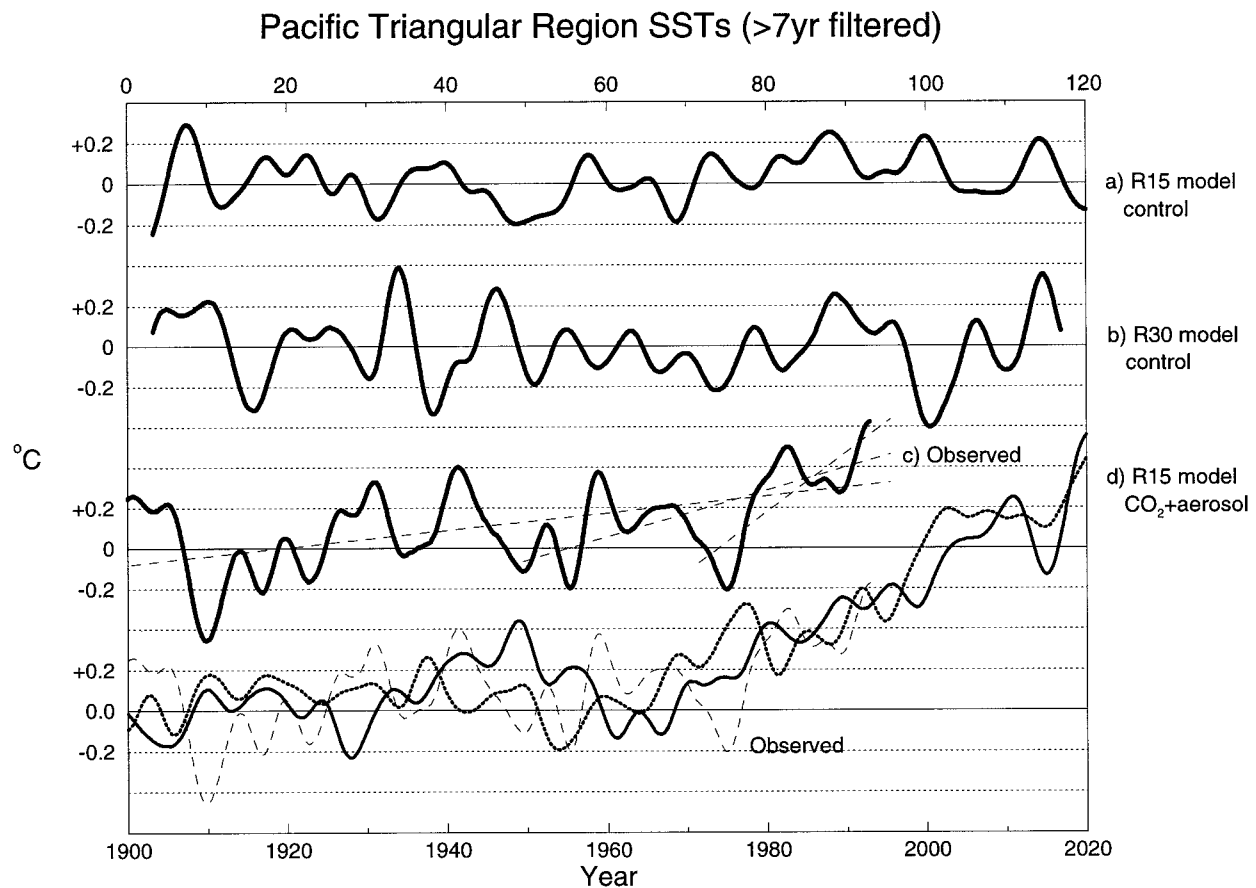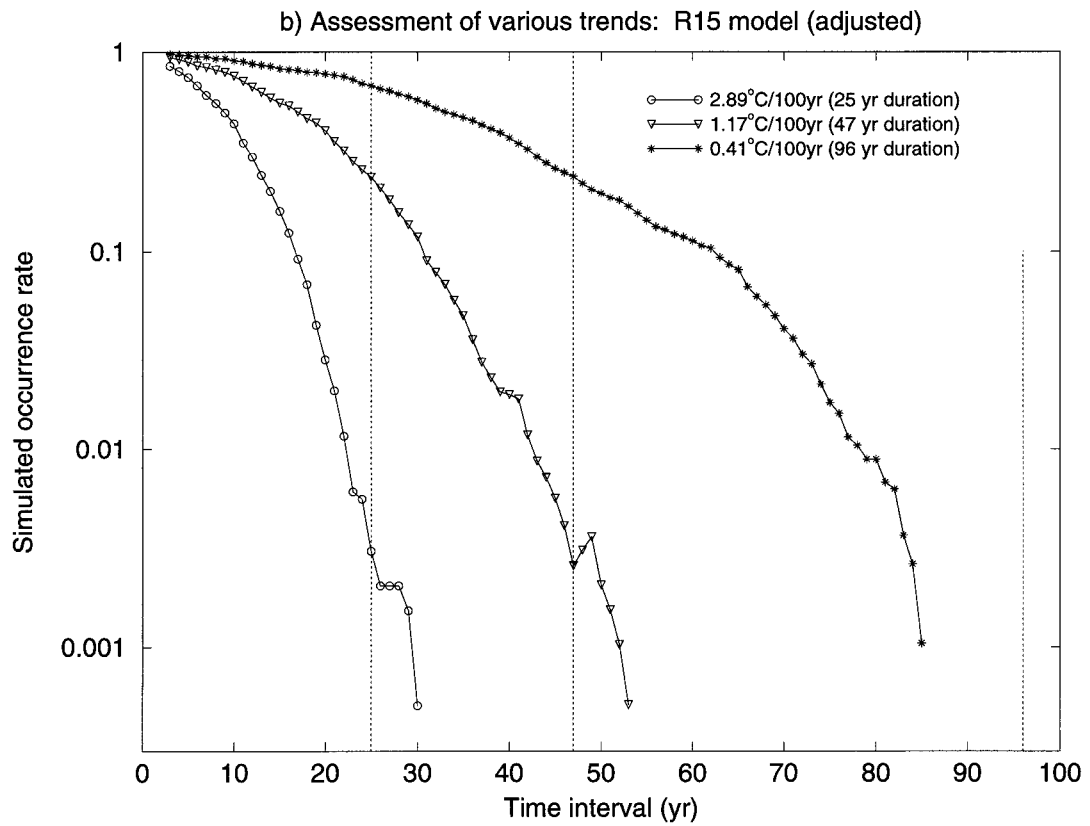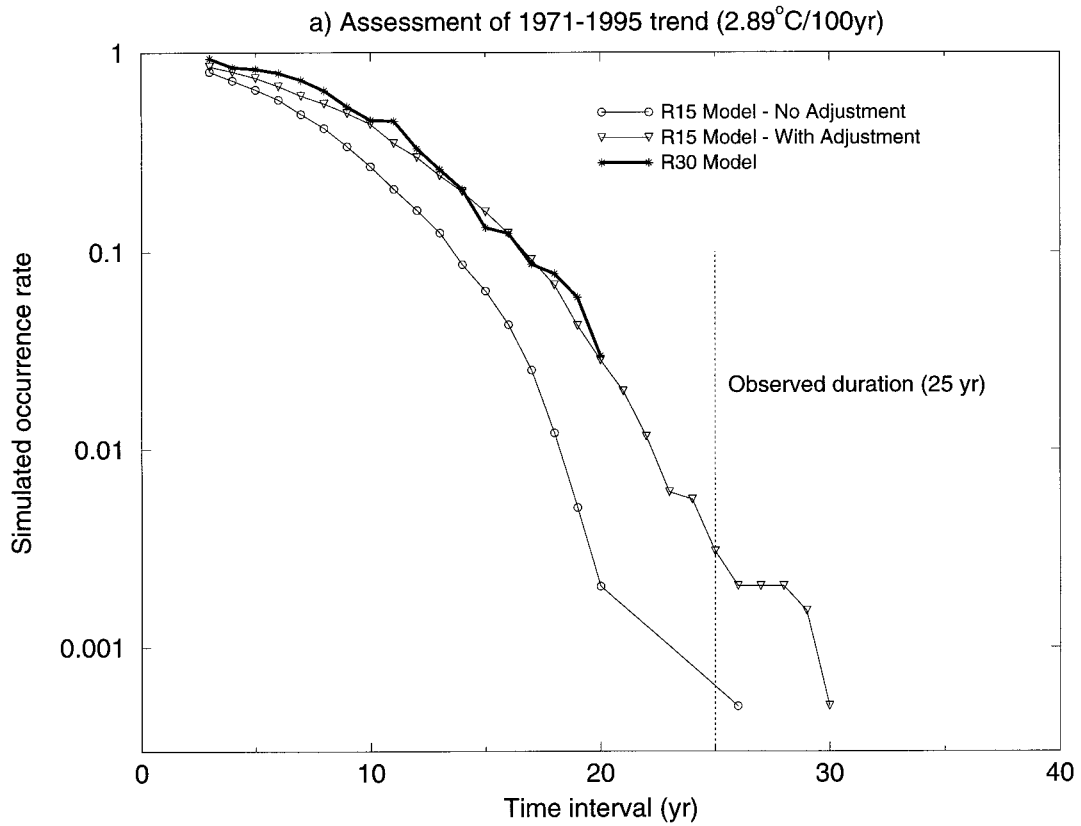## Pacific Triangular Region SSTs (>7yr filtered)

FIG. 11. (a)–(c) TPAC indices, based on area-averaged SST over the region of the Pacific encompassed by the dark line in Fig. 1. The index is shown for the (a) R15 coupled model control experiment, first 120 yr; (b) R30 coupled model control experiment; and (c) observations. The three dashed lines superimposed on (c) are the linear trends for annual mean series over the periods 1900–95, 1949–95, and 1971–95. The two darker curves labeled (d) are TPAC indices from two R15 coupled model CO_2 + aerosol experiments starting in 1765 from slightly different ocean initial conditions. The thin dashed line superimposed on them is the observed TPAC index, repeated from (c). The model and observed anomalies in (c) and (d) are deviations from the respective time means for the period 1880–1920. The TPAC indices were constructed using the same domain for the models and observation except for slight modifications due to differences in the data grid boundaries. All curves have been low-pass filtered to remove most of the variance on timescales less than 7 yr (see the appendix).

a. Assessment of trends versus internally generated variability

Figure 11c shows the observed TPAC index (>7-yr filtered), based on the MOHSST6 dataset of Parker et al. (1995) updated through February 1996. This area-averaged time series is based upon the available observations at each time period; missing data periods have not been reconstructed as with the GISST2 or Kaplan et al. SST datasets. The time series shows an upward trend from the early 1900s to the early 1940s followed by several decades with little trend, followed by a resumed upward trend beginning in the mid-1970s. The linear trend in the annual mean TPAC index is 0.41°C (100 yr)$^{-1}$ for the entire 96-yr period (1900–95), 1.2°C (100 yr)$^{-1}$ for the relatively data-rich years 1949–95, and 2.9°C (100 yr)$^{-1}$ for the most recent 25 yr (1971–95). These are illustrated by the three dashed lines superimposed on the thick curve in Fig. 11c.

The R30 coupled model TPAC index (Fig. 11b) depicts decadal variability that is greater in amplitude than that in the R15 coupled model (Fig. 11a). This is consistent with the R15 model's weaker composite decadal variability pattern noted earlier. The R30 model's internal fluctuations appear more representative of the observed variability curve in terms of typical amplitude (~0.3°C) than do the R15 model's fluctuations. In particular, the TPAC index from the R30 control run depicts some episodes that appear at least somewhat similar in duration and magnitude to the warming from the mid-1970s to the mid-1990s in the observed TPAC index. However, estimating the true level of internal variability in the observations is problematic, since the variability in the observed curve (Fig. 11c) presumably is due to not only internal climate processes, but also to various external forcings (greenhouse gases, sulfates, volcanoes, solar variability, etc.) that are not simulated in the model

a) Assessment of 1971-1995 trend (2.89°C/100yr)

b) Assessment of various trends: R15 model (adjusted)

control runs. Therefore, we cannot definitively conclude that R30 model gives a better representation of the real internal variability than the R15 model. However, the results in Figs. 11a–c and 4 strongly indicate that the observed decadal variability is closer in amplitude to the R30 model's simulated internal variability than to that of the R15 model.

We now address the question of whether the observed TPAC trends (1900–95, 1949–95, and 1971–95) are quantitatively consistent in magnitude and duration to that expected due to internal climate variability alone, using the model estimates of internal variability. If not, then our analysis would indicate that some combination of the external forcings is contributing to the observed trends. The method we use to assess the trends is to calculate the frequency of occurrence of trends of a given magnitude and duration generated in the climate model control run and compare this with the observed trend durations. This approach has been used for global surface temperature by Stouffer et al. (1994). The technique requires a long simulation, with many temporal degrees of freedom or independent trend realizations. Since we want to assess trends as long as a century in duration, we must rely on the R15 coupled model, since a multithousand-year record is not available for the R30 coupled model. The 2000-yr record of TPAC region SST from the R15 model control has a very slight long-term trend $[-0.07°C\ (1000\ yr)^{-1}]$; this trend is removed from the series before performing the assessment results described below, although not removing the trend has little impact on the assessment results.

In Fig. 12a is the model-based assessment for the observed trend of $2.9°C\ (100\ yr)^{-1}$ over the most recent 25 yr (1971–95). Following Stouffer et al. (1994), least squares linear trends are computed for all subseries of sequential years of a given length (e.g., for the 20-yr interval length, trends are computed for model years 1–20, 2–21, etc.). The distribution of the resulting trends is then plotted, for each interval length, in terms of the fraction of occurrence of trends (positive or negative) exceeding the magnitude of the observed trend $[2.9°C\ (100\ yr)^{-1}]$. The dark solid line shows the simulated rate of occurrence of such trends in the 120-yr R30 control integration. No trend of $2.9°C\ (100\ yr)^{-1}$ or more lasts longer than 20 yr in the R30 model, although the simulated record is too short to draw any firm conclusions. The curve labeled ''R15 model—no adjustment'' shows the result using a 2000-yr integration of the R15 model. The occurrence rate lies below 0.01 for intervals of 19

yr and longer, compared with the 25-yr duration of the observed trend.

A distinctive feature in Figs. 12a is that the R15 (no adjustment) curve is systematically shifted to the left of the R30 curve. As noted earlier (Figs. 11a and 11b) the internal variability in the R30 TPAC region is substantially larger than that in the R15 model and is closer to the observed decadal variability (although as mentioned above the observed series also contains noninternal variability). To illustrate the effect of the difference in variability in the models on the assessment results, the R15 model time series was adjusted by the ratio of the R30 $>$7-yr standard deviation to the R15 $>$7-yr standard deviation (a factor of 1.39), and the assessment repeated. The results, labeled ''R15 model—with adjustment'' in Fig. 12a, are in much closer agreement with the R30 model results (dark curve). These results suggest that the R15 model (with the 2000-yr available record) can be adjusted to mimic the R30 model fairly closely by scaling the anomalies as above. Although this procedure is ad hoc, we believe that the adjusted R15 series described above is likely to be more realistic than the unadjusted series. In addition, the results using the adjusted series are more conservative with regard to trend detection (i.e., one is less likely to conclude that a given observed trend is outside the range of internal variability). Therefore, for the assessments of the longer observed trends (47 and 96 yr) where the R30 model integration is clearly too short to use, we rely exclusively on the *adjusted* 2000-yr R15 model series.

In Fig. 12b are the results of the analysis, using the adjusted R15 series, for all three observed trends (i.e., 25-, 47-, and 96-yr periods ending in 1995). The results indicate that for all three of the cases, the observed trend in the TPAC index is highly unusual in the context of the model's internally generated variability. Based on all possible 25-consecutive-yr samples in the 2000-yr run, the fractional rate of occurrence of a trend of $[2.9°C\ (100\ yr)^{-1}]$ was 0.0030; for 47-yr periods $[1.2°C\ (100\ yr)^{-1}]$ the occurrence rate was 0.0026; and for 96-yr periods $[0.41°C\ (100\ yr)^{-1}$, the occurrence rate was zero in the sample, with no trend of that magnitude lasting longer than 85 yr. These sampled occurrence rates suggest that it is very unlikely that the observed trends are entirely due to natural internal variability, assuming the adjusted model-generated internal variability is a realistic representation of that expected for the real climate.

Our conclusions are similar to, though apparently not as statistically significant as, those of Stouffer et al.,

←

FIG. 12. (a) Simulated fractional occurrence rate of least squares linear trends as a function of interval length in years for a $2.89°C\ (100\ yr)^{-1}$ trend based on R15 and R30 model-simulated TPAC indices. This trend occurred in the observed annual-mean TPAC index over the most recent 25-yr period from 1971 to 1995 (see ''observed duration'' indicator on diagram). Occurrence rate results are shown for the R15 model (with unadjusted and adjusted variance) and the R30 model (unadjusted). See text for further details. (b) As in (a) but based on the adjusted R15 model series only for all three observed trends: $2.89°C\ (100\ yr)^{-1}$ (25-yr duration), $1.17°C\ (100\ yr)^{-1}$ (47-yr duration), and $0.41°C\ (100\ yr)^{-1}$ (96-yr duration).

who found no evidence that the R15 model could generate a trend in *global* surface air temperature as large as $0.5°C (100 \text{ yr})^{-1}$ for intervals longer than about 60 yr, in comparison to the 110-yr duration of their observed global trend. The apparently greater statistical significance of their result compared with ours is likely due to the fact that as smaller regions are considered (i.e., TPAC vs global), the variability in the series tends to increase; thus, the signal to noise ratio is smaller for the smaller region, making it harder to statistically distinguish a sustained climate change from the natural variability. In addition, the TPAC trend of $0.41°C (100 \text{ yr})^{-1}$ is somewhat smaller than the global surface air temperature trend ($0.5°C \ 100 \text{ yr}^{-1}$) considered by Stouffer et al. (1994).

Although global SSTs are not shown in Fig. 11, many of the features in the TPAC indices are reflected in the global average SST, for both model and observations. For example, the correlations between the TPAC index and global SST (>7-yr filtered) are 0.75, 0.77, and 0.77 for the observed, R30, and R15 data, respectively. These correlations suggest that fluctuations in global SST could be notably influenced by the TPAC region (or vice versa). An examination of the relationship between Pacific decadal variability and global SST variability (e.g., along the lines of Zhang et al. 1997) is beyond the scope of the present study, although the R30 model shows promise as a tool for addressing such issues in a future study.

b. Simulated CO_2 + aerosol warming

The possible role of anthropogenic forcing in the observed TPAC region trends is now explored. For this purpose, two simulations of twentieth-century climate change forced by anthropogenic sulfate aerosols and greenhouse gases are examined (Haywood et al. 1997). The CO_2 + aerosols forcing in these experiments represents only an estimate of the actual total radiative forcing change over the period, with many other potential forcings, such as indirect effects of aerosols upon the radiative properties of clouds, being poorly constrained at present (Schimel et al. 1995). Despite the large uncertainties in the forcing by aerosols, in the sensitivity of climate to thermal forcing, etc., these experiments appear to simulate the global mean surface air temperature change during this century quite well, which is why we have chosen to analyze the tropical SST changes from this experiment in our present study.

The dark solid and dark dotted curves in Fig. 11d show two realizations of the experiment that use the same model and radiative forcing, but begin in 1765 from slightly different ocean initial conditions. The years shown correspond to 1900–2020. Note that the thin dashed line in Fig. 11d is the observation for the TPAC region and is repeated from Fig. 11c. There is fairly good agreement between the observed TPAC index and the simulations. Both of the CO_2 + aerosol

simulations in Fig. 11d indicate a relatively gradual warming through the first half of the twentieth century, followed by a much more rapid warming ($\sim 0.2°C$ per decade) from around the 1960s through 2020. [For comparison, the warming rate in the R30 coupled model for the $+1\%$ (yr CO_2)$^{-1}$ forcing experiment without aerosols is about $0.3°C$ per decade, or roughly equivalent to the observed trend over the years 1971–95.] Note that the unusually pronounced TPAC region warm anomalies observed in the 1980s and 1990s, which are unprecedented in the available SST records, are close to the thermally forced warming level for those decades as simulated in the CO_2 + aerosol experiments. The pronounced observed warming beginning in the mid-1970s also coincides roughly in time with the apparent onset of the accelerated anthropogenic warming trend in the simulations.

The internal multidecadal variability in the R15 model apparently creates a somewhat different low-frequency evolution in the experiments, particularly from the 1940s through the 1970s. For example, one experiment (solid) shows a fairly pronounced cooling from about 1950 to 1970, with a more rapid warming trajectory apparently beginning around 1970. In the other experiment (dotted), the apparent transition to the more rapid warming trajectory is more gradual and appears to begin in the mid-1950s. If the R15 model is any guide to the relative roles of internal decadal variability and thermally forced warming in this region, then the results imply that the transition between more gradual and more rapid thermally forced warming in the real TPAC region could be difficult to identify precisely using this index because of the confounding effects of natural variability.

The more rapid warming rate in both experiments after about 1970, if it occurs in the real world, should lead to a situation where the thermally forced "signal" begins to clearly rise above the internal variability "noise" (as estimated above) within the next few decades. Whether this actually occurs or not will depend on the numerous assumptions made here, including the estimated levels of natural variability, the climate sensitivity of the real world, and the role of other radiative forcings (indirect aerosol effects, volcanic activity, solar variability, etc.) not included in these experiments.

There is little similarity between the spatial pattern of the observed trends (Figs. 1 and 4a) and the Pacific SST trend map from the R15 CO_2 + aerosol experiment (not shown). For example, while the observed trends show a cooling in the extratropical North Pacific, the R15 simulated trend patterns (for 1903–94) show a slightly enhanced warming in that region compared to the tropical Pacific. On the other hand, as mentioned previously, details of the CO_2-only warming pattern differ substantially between the R30 and R15 models. Because of this apparent sensitivity of the thermally forced patterns to model resolution, we have chosen to present here only a preliminary analysis of the R15 model CO_2 + aerosol response, based on the TPAC region alone.

A more detailed analysis, including a comparison of the spatial patterns, will be attempted once a comparable R30 CO_2 + aerosol experiment is available.

6. Summary and conclusions

In this report, we have explored possible mechanisms for observed decadal variability and trends in Pacific SSTs over the past century, including the distinctive triangular-shaped pattern of warm anomalies found in the tropical and subtropical Pacific from the late 1970s through the present. We have used the Geophysical Fluid Dynamics Laboratory global coupled ocean–atmosphere model to simulate both internal decadal variability and the response of the Pacific region to increased CO_2 or to the estimated forcing of CO_2 and aerosols combined.

a. Decadal variability—Simulated versus observed

The leading mode of decadal internally generated variability in the R30 model control run (defined in terms of EOF1 of >7-yr filtered, detrended data) is similar in amplitude and pattern to the observed decadal variability, similarly defined, as contained in the GISST2 dataset. These observed and simulated decadal variability patterns also closely resemble the observed trend in Pacific SSTs in recent decades (1949–94). The model's internal decadal variability appears to have a similar tropical delayed oscillator mechanism to that on the ENSO timescale, based on the pattern and time evolution of the model's subsurface heat content and surface wind anomalies. The westward phase propagation of heat content anomalies is slower and centered slightly farther from the equator ($\sim 12°$ vs $9°N$) for the simulated decadal variability compared to the simulated ENSO variability. This may provide at least a partial explanation (following Kirtman 1997) for the longer timescale (vs ENSO) of the simulated decadal phenomenon. The preferred timescale of the model's internal decadal events is ~ 12 yr, based on the 120-yr sample available from the R30 model. The warm tropical phase of the decadal SST variability is accompanied by cool anomalies, particularly in the north-central extratropical Pacific. An analysis of SLP and the model's surface heat budget suggests that these extratropical SST cool anomalies are a remote response to the tropical SST anomalies via an ''atmospheric bridge.'' On the decadal timescale, the extratropical atmospheric surface wind anomalies appear to induce a local SST cooling in part by modifying the three-dimensional ocean near-surface current structure that results in anomalous advective cooling. This is in distinct contrast to the model's ENSO timescale variability, where the extratropical cooling is produced mainly by surface heat flux anomalies.

b. Simulated CO_2-warming pattern

The pattern of CO_2-induced Pacific warming in the higher-resolution (R30) model has a broader, more triangular shaped structure and emerges from the model's internal variability more quickly (~ 50 yr) than the tropical Pacific warming pattern simulated in the lower-resolution (R15) model analyzed by Knutson and Manabe (1995). By comparing the R30 coupled model pattern to that from an R30 experiment with a simple mixed layer ocean, the interactive ocean dynamics is seen to produce decreased upwelling and a locally enhanced warming over the central and western equatorial Pacific. Apart from that feature, much of the triangular structure in the R30 coupled model's Pacific warming pattern is also present in the mixed layer model and thus apparently does not depend crucially on interactive ocean dynamics. Although several mechanisms appear to contribute to these features of the models' response, the overall change can be characterized as a slight CO_2-induced decrease in the Walker circulation and Pacific trade wind system, as found for the R15 model by Knutson and Manabe (1995). The R30 coupled model's CO_2-induced warming pattern shows some similarity to the simulated internal decadal variability ($r_{xy} = 0.55$), although a clear distinction is that the model's CO_2-induced pattern is more spatially uniform and is of one sign (positive) over the entire Pacific domain. The similarity in the model trend and decadal variability patterns suggests (by analogy) that in the real world, the CO_2-induced warming might be expected to share some spatial characteristics with the observed decadal variability. This could complicate efforts to distinguish between a CO_2-induced warming and natural decadal variability on the basis of the SST patterns alone.

c. Interpretation of observed trends

A trend map for observed SSTs from 1949 to 1994 shows warming in a broad triangular-shaped region centered in the tropical Pacific (TPAC region), flanked by cooling trends in the extratropical Pacific. The century-scale trend (1900–94) in the GISST2 data indicates warming over most of the Pacific, with only a few regions of cooling—located away from the equatorial Pacific—and a relatively pronounced warming in the TPAC region. The century-scale trend should be considered less reliable than the 1949–94 trend since the SST reconstruction is less reliable for the pre-1949 period. An index of observed SST averaged over the TPAC region indicates warming trends of $+0.41°C$ $(100 \text{ yr})^{-1}$ since 1900, $+1.2°C$ $(100 \text{ yr})^{-1}$ since 1949, and $+2.9°C$ $(100 \text{ yr})^{-1}$ since 1971. The simulations of internal variability presented here show examples of periods resembling the observed trend of the last 25 yr, indicating that natural variability potentially could have accounted for much of the warming in the region in recent decades. However, a quantitative comparison of simulated and

observed trends indicates that the durations of the observed trends are highly unusual in the context of model-generated internal variability for the region. All three of the observed trends mentioned above have occurrence rates of less than 0.5% in an adjusted 2000-yr record of internal variability from a low-resolution coupled model. The observed trend since 1900 [$0.41°C$ $(100 \text{ yr})^{-1}$, 96-yr duration] is the most unusual, with the longest simulated trend of that magnitude lasting only 85 yr. These results suggest that the TPAC region trends are not entirely attributable to natural internal variability alone but may have resulted in part from a sustained thermal forcing, such as that due to greenhouse gases, aerosol loading, or solar variability. Our assessment of recent tropical Pacific SST changes as highly unusual and our model's weaker Walker circulation in response to increased CO_2 are reminiscent of Trenberth and Hoar's (1996) conclusion that the recent Southern Oscillation behavior is unlikely to have been a result of natural variability alone.

To quantitatively assess of the potential role of thermal forcing in the warming of the TPAC region over the past century, we have examined two low-resolution (R15) model simulations forced with estimated past concentrations of greenhouse gases and tropospheric sulfate aerosols, as these experiments appear to simulate changes in global temperature over the past century quite well (Haywood et al. 1997). The TPAC indices from these simulations track the observed TPAC index fairly well. The pronounced warm anomalies observed in the TPAC region during the 1980s and 1990s, which are unprecedented in the available SST records, are close to the thermally forced warming level for those decades as simulated in the CO_2 + aerosol experiments. Thus, these results suggest that essentially all of the recent TPAC region warming could potentially be attributable to thermal forcing.

At present, we are not able to determine what fraction of the observed eastern tropical Pacific warming is actually due to natural variability or to thermal forcing. The observed cooling trends in the extratropical North Pacific (Fig. 1) are not evident in the thermally forced trend field in our CO_2 + aerosol simulations. Rather, these cooling trends may be related to the R30 model's internal decadal variability described here or to extratropical multidecadal variability similar to the EOF2 mode of Deser and Blackmon (1995). However, it is difficult to infer how much of the recent tropical warming is due to natural variability based upon the extratropical North Pacific cooling, since some forms of North Pacific variability (such as the internal decadal variability described in this report, or EOF1 of Deser and Blackmon) are strongly linked to the Tropics while other forms (e.g., EOF2 of Deser and Blackmon) appear not to be. In addition, similarities in the spatial structure of our model's internal decadal variability and CO_2-warming patterns complicate the use of pattern-based techniques such as conventional EOF analysis to distinguish natural variability and thermally forced signals over the Pacific region.

In summary, our model results indicate that the observed warming trend in the eastern tropical Pacific is not likely to be solely attributable to internal (natural) climate variability. Instead, it is likely that a sustained thermal forcing, such as the increase of greenhouse gases in the atmosphere, has been at least partly responsible for the observed warming.

APPENDIX

Time Filter Design

To separate variability associated with El Niño–Southern Oscillation (ENSO) from decadal- and longer-scale variability, a 73-weight finite impulse response low-pass filter with a Chebyshev window was applied to the data after removal of the mean seasonal cycle. This filter was designed using the MATLAB digital filter design software. The filter has a magnitude response at 3, 5, 7, 10, and 20 yr of 0.03, 0.3, 0.6, 0.8, and 0.94, respectively. In designing the filter to have both a desirable frequency response curve with a minimal loss of data at the ends of the record, a 30-dB ripple was allowed. This compromise resulted in some residual high-frequency noise in the filtered data that was suppressed using a separate application of a 5-month running mean filter. The same filtering technique was applied to both observed and model data. The low-pass filter is very roughly equivalent to a 5-yr running mean filter (although without many of the undesirable frequency response features of such a filter). Thus the individual "events" in our composites are roughly equivalent to 5-yr averages centered on the composite dates.

The choice of 7 yr as the approximate dividing line between ENSO and decadal variability is somewhat arbitrary and is based on examination of the spectra of the first principal components for both the model and observed detrended monthly anomalies. The observed SST spectra has the strongest peaks at about 5 and 3.5 yr, with a smaller peak at about 12 yr. The R30 model spectra have the strongest peaks at about 12 and 7 yr, with a smaller peak at about 4 yr. A separate spectral analysis for 10 separate 92-yr segments of a 1000-yr R15 coupled model experiment showed a strongest "average" peak at about 12 yr but with considerable scatter in the location and magnitude of the spectral peaks

among the separate 92-yr segments. This suggests that the detailed structure of the observed and R30 spectra probably should not be interpreted too literally on the basis of only a century-long record. We conclude that for the purpose of our analysis, 7 yr is a reasonable dividing line between the ''conventional wisdom'' ENSO timescale (roughly 2–6 yr) and the longer-scale variability, although the true timescale of ENSO appears to still be an open question. As for the real world, the timescale of internal Pacific variability is still uncertain, since the contribution of external forcing to the observed decadal- to century-scale variability cannot yet be unambiguously distinguished.

As a test of the sensitivity of our results to the choice of filter bands, we repeated the composite analysis using a second filter that used 241 weights and had a magnitude response at 5, 7, 10, and 20 yr of 0.003, 0.06, 0.51, and 0.99, respectively. Using this lower-pass (>10 yr) filter, the compositing procedure selects fewer events (two warm and two cold cases), but the composite warm–cold anomalies are similar to those for the larger set of events obtained using the >7-yr filter.

REFERENCES

Alexander, M. A., 1990: Simulation of the response of the North Pacific Ocean to the anomalous atmospheric circulation associated with El Niño. *Climate Dyn.,* **5,** 53–65.

Battisti, D. S., and A. C. Hirst, 1989: Interannual variability in a tropical atmosphere–ocean model: Influence of the basic state, ocean geometry and nonlinearity. *J. Atmos. Sci.,* **46,** 1687–1712.

Cane, M. A., M. Munnich, and S. E. Zebiak, 1990: A study of self-excited oscillations of the tropical ocean–atmosphere system. Part I: Linear analysis. *J. Atmos. Sci.,* **47,** 1562–1577.

——, A. C. Clement, A. Kaplan, Y. Kushnir, R. Murtugudde, D. Pozdnyakov, R. Seager, and S. E. Zebiak, 1997: 20th century sea surface temperature trends. *Science,* **275,** 957–960.

Chao, Y., and S. G. H. Philander, 1993: On the structure of the Southern Oscillation. *J. Climate,* **6,** 450–469.

Clement, A. C., R. Seager, M. A. Cane, and S. E. Zebiak, 1996: An ocean dynamical thermostat. *J. Climate,* **9,** 2190–2196.

Deser, C., and M. L. Blackmon, 1995: On the relationship between Tropical and North Pacific sea surface temperature variations. *J. Climate,* **8,** 1677–1680.

——, M. A. Alexander, and M. S. Timlin, 1996: Upper-ocean thermal variations in the North Pacific during 1970–1991. *J. Climate,* **9,** 1840–1855.

Graham, N. E., 1994: Decadal-scale climate variability in the tropical and North Pacific during the 1970s and 1980s: Observations and model results. *Climate Dyn.,* **10,** 135–162.

——, 1995: Simulation of recent global temperature trends. *Science,* **267,** 666–671.

——, and W. B. White, 1988: The El Niño cycle: A natural oscillator of the Pacific ocean–atmosphere system. *Science,* **240,** 1293–1302.

Gu, D., and S. G. H. Philander, 1997: Interdecadal climate fluctuations that depend on exchanges between the Tropics and extratropics. *Science,* **275,** 805–807.

Gutzler, D. S., 1996: Low-frequency ocean–atmosphere variability across the tropical western Pacific. *J. Atmos. Sci.,* **53,** 2773–2785.

Haywood, J. M., R. J. Stouffer, R. T. Wetherald, S. Manabe, and V. Ramaswamy, 1997: Transient response of a coupled model to estimated changes in greenhouse gas and sulfate concentrations. *Geophys. Res. Lett.,* **24,** 1335–1338.

Houghton, J. T., B. A. Callander, and S. K. Varney, Eds., 1992: *Climate Change 1992: The Supplementary Report to the IPCC Scientific Assessment.* Cambridge University Press, 198 pp.

Kachi, M., and T. Nitta, 1997: Decadal variations of the global atmosphere–ocean system. *J. Meteor. Soc. Japan,* **75,** 657–675.

Kaplan, A., Y. Kushner, M. A. Cane, and M. B. Blumenthal, 1997: Reduced space optimal analysis for historical data sets: 136 years of Atlantic sea surface temperatures. *J. Geophys. Res.,* **102** (C13), 27 835–27 860.

Kirtman, B. P., 1997: Oceanic Rossby wave dynamics and the ENSO period in a coupled model. *J. Climate,* **10,** 1690–1704.

Knutson, T. R., and S. Manabe, 1995: Time-mean response over the tropical Pacific to increased CO_2 in a coupled ocean–atmosphere model. *J. Climate,* **8,** 2181–2199.

——, ——, and D. Gu, 1997: Simulated ENSO in a global coupled ocean–atmosphere model: Multidecadal amplitude modulation and CO_2 sensitivity. *J. Climate,* **10,** 138–161.

Latif, M., and T. P. Barnett, 1996: Decadal climate variability over the North Pacific and North America: Dynamics and predictability. *J. Climate,* **9,** 2407–2423.

——, R. Kleeman, and C. Eckert, 1997: Greenhouse warming, decadal variability, or El Niño? An attempt to understand the anomalous 1990s. *J. Climate,* **10,** 2221–2239.

Lau, N.-C., and M. J. Nath, 1996: The role of the ''atmospheric bridge'' in linking tropical Pacific ENSO events to extratropical SST anomalies. *J. Climate,* **9,** 2036–2057.

Lindberg, C., and A. J. Broccoli, 1996: Representation of topography in spectral climate models and its effect on simulated precipitation. *J. Climate,* **9,** 2641–2659.

Manabe, S., and R. J. Stouffer, 1994: Multiple-century response of a coupled ocean–atmosphere model to an increase of atmospheric carbon dioxide. *J. Climate,* **7,** 5–23.

——, ——, M. J. Spelman, and K. Bryan, 1991: Transient response of a coupled ocean–atmosphere model to gradual changes of atmospheric CO_2. Part I: Annual mean response. *J. Climate,* **4,** 785–818.

McCreary, J. P., 1983: A model of tropical ocean–atmosphere interaction. *Mon. Wea. Rev.,* **111,** 370–387.

Meehl, G. A., and W. M. Washington, 1996: El Niño-like climate change in a model with increased atmospheric CO_2 concentrations. *Nature,* **382,** 56–60.

——, and J. M. Arblaster, 1998: The Asian–Australian monsoon and El Niño–Southern Oscillation in the NCAR Climate System Model. *J. Climate,* **11,** 1357–1387.

——, W. M. Washington, D. J. Erickson III, B. P. Briegleb, and P. J. Jaumann, 1996: Climate change from increased CO_2 and direct and indirect effects of sulfate aerosols. *Geophys. Res. Lett.,* **23,** 3755–3758.

Miller, A. J., D. R. Cayan, T. P. Barnett, N. E. Graham, and J. M. Oberhuber, 1994: Interdecadal variability of the Pacific Ocean: Model response to observed heat flux and wind stress anomalies. *Climate Dyn.,* **10,** 135–162.

Mitchell, J. F. B., T. C. Johns, J. M. Gregory, and S. F. B. Tett, 1995: Climate response to increasing levels of greenhouse gases and sulfate aerosols. *Nature,* **376,** 501–504.

Nicholls, N., G. V. Gruza, J. Jouzel, T. R. Karl, L. A. Ogallo, and D. E. Parker, 1995: Observed climate variability and change. *Climate Change 1995: The Science of Climate Change,* J. T. Houghton, L. G. Meira Filho, B. A. Callander, N. Harris, A. Kattenberg, and K. Maskell, Eds., Cambridge University Press, 133–192.

Nitta, T., and S. Yamada, 1989: Recent warming of tropical sea surface temperature and its relationship to the Northern Hemisphere circulation. *J. Meteor. Soc. Japan,* **67,** 375–383.

Parker, D. E., P. D. Jones, C. K. Folland, and A. Bevan, 1994: Interdecadal changes of surface temperature since the late nineteenth century. *J. Geophys. Res.,* **99** (D7), 14 373–14 399.

——, C. K. Folland, and M. Jackson, 1995: Marine surface temperature: Observed variations and data requirements. *Climate Change,* **31,** 559–600.

Rasmusson, E. M., and T. H. Carpenter, 1982: Variations in tropical sea surface temperature and surface wind fields associated with the Southern Oscillation–El Niño. *Mon. Wea. Rev.,* **110,** 354–384.

Rayner, N. A., E. B. Horton, D. E. Parker, C. K. Folland, and R. B. Hackett, 1996: Version 2.2 of the global sea-ice and sea surface temperature data set, 1903–1994. UKMO Climate Research Tech. Note CRTN74, 46 pp. [Available from National Meteorological Library, Meteorological Office, London Rd., Bracknell, Berkshire RG12 2SY, United Kingdom.]

Schimel, D., and Coauthors, 1995: Radiative forcing of climate change. *Climate Change 1995: The Science of Climate Change,* J. T. Houghton, L. G. Meira Filho, B. A. Callander, N. Harris, A. Kattenberg, and K. Maskell, Eds., Cambridge University Press, 65–131.

Schneider, E. K., B. Huang, and J. Shukla, 1995: Ocean wave dynamics and El Niño. *J. Climate,* **8,** 2415–2439.

——, R. S. Lindzen, and B. P. Kirtman, 1997: A tropical influence on global climate. *J. Atmos. Sci.,* **54,** 1349–1358.

Schopf, P. S., and M. J. Suarez, 1988: Vacillations in a coupled ocean–atmosphere model. *J. Atmos. Sci.,* **45,** 549–566.

——, and ——, 1990: Ocean wave dynamics and the time scale of ENSO. *J. Phys. Oceanogr.,* **20,** 629–645.

Seager, R., and R. Murtugudde, 1997: Ocean dynamics, thermocline adjustment and regulation of tropical SST. *J. Climate,* **10,** 521–539.

Stouffer, R. J., S. Manabe, and K. Y. Vinnikov, 1994: Model assessment of the role of natural variability in recent global warming. *Nature,* **367,** 634–636.

Tett, S., 1995: Simulation of El Niño–Southern Oscillation-like variability in a global AOGCM and its response to CO_2 increase. *J. Climate,* **8,** 1473–1502.

Trenberth, K. E., 1990: Recent observed interdecadal climate changes in the Northern Hemisphere. *Bull. Amer. Meteor. Soc.,* **71,** 988–993.

——, and D. A. Paolino Jr., 1980: The Northern Hemisphere sea-level pressure data set: Trends, errors and discontinuities. *Mon. Wea. Rev.,* **108,** 855–872.

——, and J. W. Hurrell, 1994: Decadal atmosphere–ocean variations in the Pacific. *Climate Dyn.,* **9,** 303–319.

——, and T. J. Hoar, 1996: The 1990–1995 El Niño–Southern Oscillation Event: Longest on record. *Geophys. Res. Lett.,* **23,** 57–60.

Wallace, J. M., and D. S. Gutzler, 1981: Teleconnections in the geopotential height field during the Northern Hemisphere winter. *Mon. Wea. Rev.,* **109,** 784–812.

Wetherald, R. T., 1996: Feedback processes in the GFDL R30-14 level general circulation model. *Climate Sensitivity to Radiative Perturbations: Physical Mechanisms and Their Validation,* H. Le Treut, Ed., NATO ASI Series, Vol. I34, Springer-Verlag, 251–266.

Yukimoto, S., M. Endoh, Y. Kitamura, A. Kitoh, T. Motoi, A. Noda, and T. Tokioka, 1996: Interannual and interdecadal variabilities in the Pacific in an MRI coupled GCM. *Climate Dyn.,* **12,** 667–683.

Zebiak, S. E., and M. A. Cane, 1987: A model El Niño–Southern Oscillation. *Mon. Wea. Rev.,* **115,** 2262–2278.

Zhang, Y., J. M. Wallace, and D. S. Battistsi, 1997: ENSO-like interdecadal variability: 1900–93. *J. Climate,* **10,** 1004–1020.